Spinal Motoneuron TMEM16F Acts at C-boutons to Modulate Motor Resistance and Contributes to ALS Pathogenesis

Claire Soulard, Céline Salsac, Kevin Mouzat, Cécile Hilaire, Julien Roussel, Alexandre Mezghrani, Serge Lumbroso, Cédric Raoul, Frédérique Scamps

Article

Cell Reports

Spinal Motoneuron TMEM16F Acts at C-boutons to Modulate Motor Resistance and Contributes to ALS Pathogenesis

Graphical Abstract

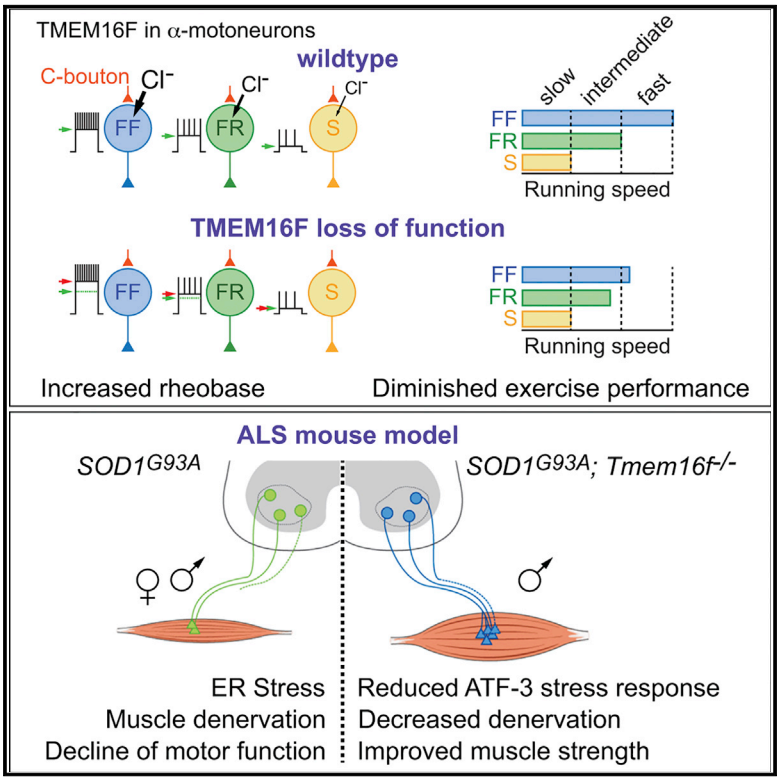

Highlights

- TMEM16F locates at cholinergic inputs in motoneurons
- TMEM16F controls the recruitment threshold of fast α-motoneurons
- Loss of TMEM16F chloride conductance reduces performance to demanding motor exercise
- TMEM16F loss of function in ALS mice reduces denervation and motor decline

Authors

Claire Soulard, Céline Salsac, Kevin Mouzat, ..., Serge Lumbroso, Cédric Raoul, Frédérique Scamps

Correspondence

cedric.raoul@inserm.fr (C.R.), frederique.scamps@inserm.fr (F.S.)

In Brief

Soulard et al. show that TMEM16F, a calcium-activated chloride channel, is a post-synaptic component of C-boutons that contributes to the excitability of fast α-motoneurons. They find that the loss of TMEM16F function leads to reduced performance during motor-demanding tasks but improves motor functions of male mice with amyotrophic lateral sclerosis.

Soulard et al., 2020, Cell Reports *30*, 2581–2593
February 25, 2020
https://doi.org/10.1016/j.celrep.2020.02.001

CellPress

Cell Reports
Article

Spinal Motoneuron TMEM16F Acts at C-boutons to Modulate Motor Resistance and Contributes to ALS Pathogenesis

Claire Soulard,[1] Céline Salsac,[1] Kevin Mouzat,[1,2] Cécile Hilaire,[1] Julien Roussel,[1] Alexandre Mezghrani,[1] Serge Lumbroso,[1,2] Cédric Raoul,[1,3,*] and Frédérique Scamps[1,3,4,*]

[1]The Neuroscience Institute of Montpellier, INM, INSERM UMR1051, University of Montpellier, Saint-Eloi Hospital, 80 rue Augustin Fliche, 34091 Montpellier, France

[2]Laboratoire de Biochimie et Biologie Moléculaire, CHU Nîmes, University of Montpellier, 4 Rue du Professeur Robert Debré, 30029 Nîmes, France

[3]These authors contributed equally

[4]Lead Contact

*Correspondence: cedric.raoul@inserm.fr (C.R.), frederique.scamps@inserm.fr (F.S.)

https://doi.org/10.1016/j.celrep.2020.02.001

SUMMARY

Neuronal Ca^{2+} entry elicited by electrical activity contributes to information coding via activation of K^+ and Cl^- channels. While Ca^{2+}-dependent K^+ channels have been extensively studied, the molecular identity and role of Ca^{2+}-activated Cl^- channels (CaCCs) remain unclear. Here, we demonstrate that TMEM16F governs a Ca^{2+}-activated Cl^- conductance in spinal motoneurons. We show that TMEM16F is expressed in synaptic clusters facing pre-synaptic cholinergic C-boutons in α-motoneurons of the spinal cord. Mice with targeted exon deletion in *Tmem16f* display decreased motor performance under high-demanding tasks attributable to an increase in the recruitment threshold of fast α-motoneurons. Remarkably, loss of TMEM16F function in a mouse model of amyotrophic lateral sclerosis (ALS) significantly reduces expression of an activity-dependent early stress marker and muscle denervation, delays disease onset, and preserves muscular strength only in male ALS mice. Thus, TMEM16F controls motoneuron excitability and impacts motor resistance as well as motor deterioration in ALS.

INTRODUCTION

Spinal motoneurons are responsible for the contraction of skeletal muscle and must adapt to exercise-dependent demands. The recruitment threshold of motoneurons is a major determinant for task-dependent demands. Identification of different thresholds has led to the identification of three main subpopulations of α-motoneurons. Slow motoneurons have a low recruitment threshold and contribute to standing. Fast motoneurons are involved in task demands and are subdivided into fast-fatigable (FF) and fatigue-resistant (FR) categories, with FF motoneurons having a higher recruitment threshold than FR neurons (Burke et al., 1973; Gustafsson and Pinter, 1984). The functional peculiarity of motoneuron types is further evidenced in the neurodegenerative disease amyotrophic lateral sclerosis (ALS), which features a sequential loss of motoneurons, beginning with high-threshold FF motoneurons and followed by medium-threshold FR motoneurons; the low-threshold S motoneurons are preserved (de Carvalho et al., 2014; Kanning et al., 2010). This preferential motoneuron loss led to the hypothesis that biophysical properties of motoneuron types could be a determinant in ALS onset. Altogether, these observations highlight the need to continue the identification of the molecular actors controlling motoneuron recruitment.

Ca^{2+}-activated Cl^- channels (CaCCs) are widely expressed in central and peripheral neurons, and since the discovery of the *Tmem16/Anoctamin* family genes, their role as potential regulators of neuronal excitability is beginning to emerge (Caputo et al., 2008; Schroeder et al., 2008; Yang et al., 2008). Among the 10 members of the TMEM16 family (Hartzell et al., 2009), TMEM16B has been identified as an actor in synaptic activity in hippocampal neurons (Huang et al., 2012); it also mediates spike frequency adaptation in thalamocortical neurons (Ha et al., 2016) and contributes to neuronal firing of inferior olivary neurons (Zhang et al., 2017). TMEM16A and TMEM16C are contributors of potential generator and firing properties, respectively, in pain-sensing neurons (Cho et al., 2012; Liu et al., 2010; Yang et al., 2008). While it has long been reported that CaCCs are found in spinal cords, the expression, molecular identity, and role of these channels in motoneurons have never been addressed.

We show that TMEM16F is responsible for a Ca^{2+}-activated Cl^- conductance recorded in spinal motoneurons. TMEM16F is located in α-motoneurons facing C-boutons synapses in spinal cords, and its loss of function decreases forced locomotor performance. *In situ* recordings of electrical activity of motoneurons with targeted exon deletion in *Tmem16f* reveal an increase in recruitment threshold of the fast motoneuron population. In mice expressing the ALS-causing $SOD1^{G93A}$ mutant, loss of TMEM16F function reduces the expression of the activity-regulated stress marker ATF3, delays disease onset, and prevents muscle performance decline during disease progression, only in male mice.

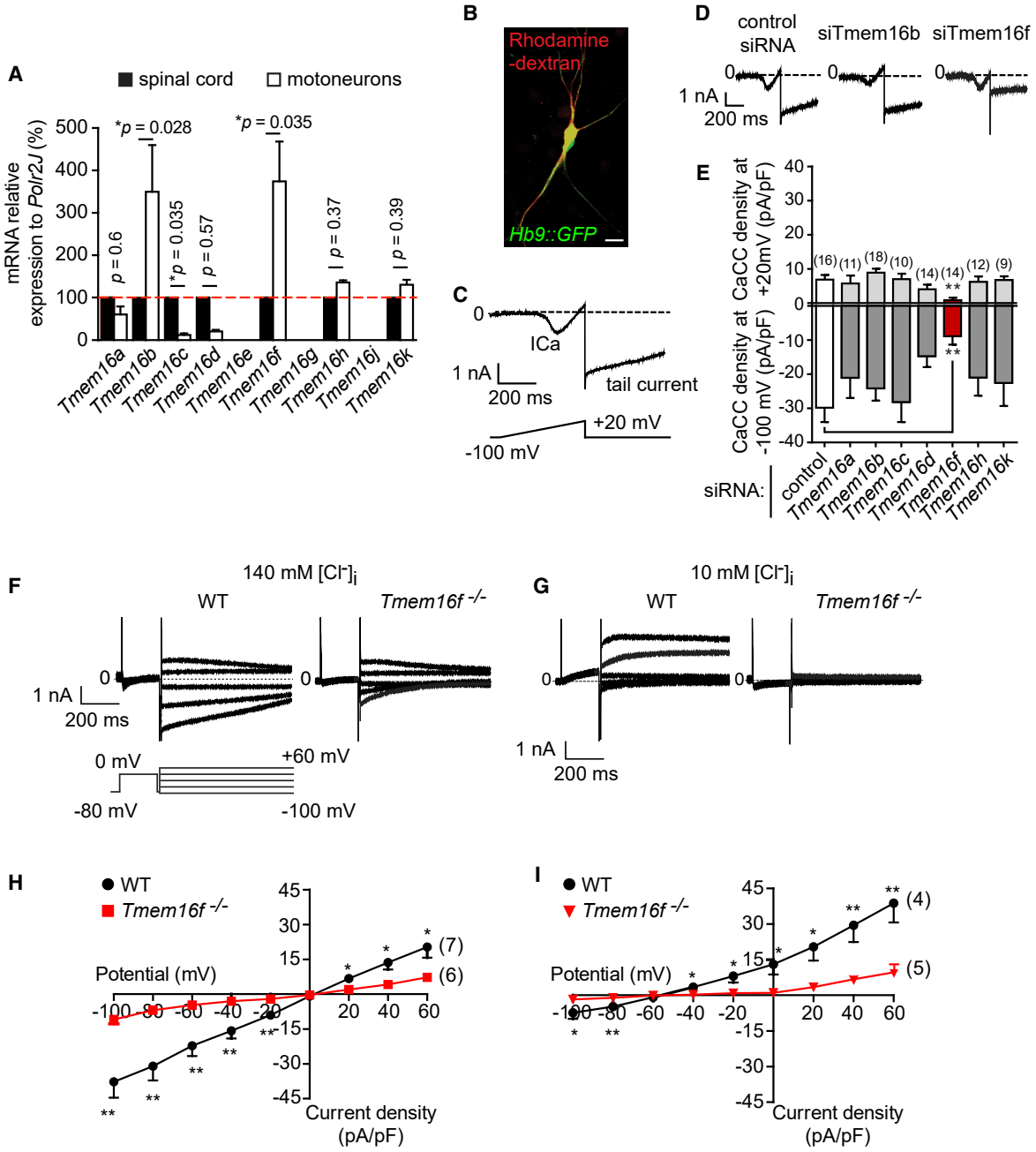

Figure 1. TMEM16F Contributes to Ca^{2+}-Activated Cl^- Currents in Motoneurons

(A) Real-time RT-PCR was performed on total RNA isolated from the spinal cord of 2-month-old wild-type mice and purified motoneurons at 7 DIV. Transcript levels of *Tmem16a–k* were expressed relative to relative to *polymerase (RNA) II polypeptide J* (*Polr2J*) transcript (n = 4; *p < 0.05, Mann-Whitney test).

(B) Representative image of a 10 DIV *Hb9::GFP* motoneuron (green) 2 days after single-cell electroporation with dextran-rhodamine/siRNA complexes (red). Scale bar, 20 μm.

(C) A ramp protocol was used to screen for activation of a tail current on repolarization to −100 mV, under isotonic 140 mM [Cl^-].

(D) Representative current traces obtained following electroporation of motoneurons with irrelevant control siRNA or siRNA directed against *Tmem16b* and *Tmem16f* RNA.

(E) A significant decrease in inward tail amplitude at −100 mV and in outward current at +20 mV is obtained in siTmem16f-electroporated motoneurons compared with control siRNA. Numbers in brackets indicate the number of motoneurons; **p < 0.01, one-way ANOVA followed by Dunnett's post hoc test.

(F–I) Current-voltage relationships of the tail current in wild-type (WT) and *Tmem16f*$^{-/-}$ motoneurons. Following voltage-gated Ca^{2+} channel (I_{Ca}) activation at 0 mV, tail currents are recorded in 20-mV increments from −100 to +60 mV every 10 s.

(legend continued on next page)

RESULTS

TMEM16F Contributes to Ca^{2+}-Activated Cl^- Conductance in Spinal Motoneurons

To characterize the molecular identity of CaCCs, we determined expression levels of the 10 *Tmem16* family members and the 3 *Bestrophin* family members in the mouse spinal cord and purified motoneurons. Using quantitative RT-PCR, we found that, with the exception of *Tmem16e*, *Tmem16g*, and *Tmem16j*, all transcripts were expressed in the spinal cords and purified motoneurons (Figure 1A). The expression of *Tmem16b* and *Tmem16f* were significantly enriched in motoneurons relative to spinal cords, while *Tmem16c* was significantly enriched in spinal cords relative to purified motoneurons. These results were further confirmed using *Gapdh* as another reference gene (Figure S1A). There were no significant differences in the expression of *Tmem16a*, *Tmem16d*, *Tmem16h*, and *Tmem16k* between spinal cords and motoneurons. Among the *Bestrophin* family, *Best 2* was not found to be expressed. *Best 1* and *Best 3* had a trend toward an enrichment in spinal cords, a result consistent with the function of Best 1 in astrocytes (Woo et al., 2012) (Figure S1B). We next performed electrophysiological recordings to assess Ca^{2+}-activated Cl^- conductance CaCC in *Hb9::GFP* motoneurons at 7–8 days *in vitro* (DIV). Extracellular replacement of Na^+ and K^+ with N-methyl-D-glucamine and intracellular K^+ substitution with Cs^+ were used to prevent activation of Na^+ and K^+ currents. Under these conditions, voltage ramps applied from −100 to +20 mV activated voltage-gated Ca^{2+} current (I_{Ca}). We observed activation of an outward current at depolarized values followed by a tail inward current on repolarization to −100 mV in 75% of motoneurons (Figures S1C–S1E). Application of the Cl^- channel inhibitor niflumic acid (NFA) decreased both the outward and tail inward current amplitudes (Figures S1D and S1F). The replacement of Ca^{2+} by Ba^{2+} prevented activation of the tail current, thus confirming the Ca^{2+} dependence of the current (Figures S1G–S1I). To determine which TMEM16 contributes to the Ca^{2+}-activated tail current in motoneurons, we performed an RNA inhibition strategy using single-cell electroporation of small interfering RNAs (siRNAs) (Boudes et al., 2008). Following electroporation of *Hb9::GFP* motoneurons with siRNAs together with dextran-rhodamine at 7–8 DIV, the rhodamine-positive motoneurons were recorded 2 days later using a ramp protocol (Figures 1B and 1C). Analysis of the outward current at +20 mV and the tail current densities showed that among the seven *Tmem16* genes expressed in motoneurons, only siRNA directed against *Tmem16f* induced a significant decrease in outward and inward currents (Figures 1D and 1E). Under 140 mM isotonic $[Cl^-]_i$, the current-voltage relationships of the tail current showed a linear conductance with an apparent reversal potential (E_{rev}) of around 0 mV, which shifted to hyperpolarized potential (−60 mV) and displayed outwardly rectifying properties when using 10 mM $[Cl^-]_i$ (Figures 1F–1I). Of note, using low intracellular $[Cl^-]$, activation of mouse TMEM16F expressed in HEK293T cells by addition of the Ca^{2+} ionophore ionomycin does also elicit an outwardly rectifying current with a reversal potential that suggests a favored permeation to Cl^- of this channel (Figures S1J and S1K). In motoneurons purified from mice with targeted deletion of exon 3 in *Tmem16f* (referred as *Tmem16f*$^{-/-}$) (Yang et al., 2012) (Figure S2A), and that still lead to the production of N-terminal truncated TMEM16F variants (Figures S2B–S2H), the tail current amplitude was consistently significantly decreased under high or low $[Cl^-]_i$ (Figures 1F–1I), demonstrating that TMEM16F contributes to the functional expression of a CaCC in motoneurons.

TMEM16F Is Expressed by α-Motoneurons at Cholinergic Inputs

To determine TMEM16F expression profile in the adult mouse spinal cord, we tested the ability of several antibodies to recognize mouse TMEM16F and validated an antibody directed against the extracellular part of TMEM16F (Figure S2G). In spinal cord, TMEM16F was observed specifically in choline acetyl transferase-positive ($ChAT^+$) motoneurons located in the ventral horn laminae VIII and IX (Figure 2A). No signal was observed in other laminae of the ventral or dorsal horn. TMEM16F staining appeared as clusters mainly at the plasma membrane of soma and dendrites of medial and lateral $ChAT^+$ motoneurons (Figures 2A and 2B). No staining was detected at the neuromuscular junction (not shown). To identify the subtype of motoneurons expressing TMEM16F, we performed co-staining with ChAT, a pan-cholinergic neuron marker, and estrogen-related receptor gamma (ERRγ), a specific marker of γ-fusimotor neurons (Figure 2C). We observed that the vast majority of γ-fusimotor neurons, which represents approximately 23% of $ChAT^+$ motoneurons, does not express TMEM16F (Figures 2D and 2E). The 77% of ERRγ-negative ($ERR\gamma^-$) motoneurons include mainly α-motoneurons and 90% of them express TMEM16F (Figures 2D and 2E). Co-staining with the Na^+/K^+-ATPase α1 subunit, a plasma membrane marker of motoneurons (Bowerman et al., 2017; Edwards et al., 2013), indicated membrane localization of TMEM16F in motoneurons (Figure 2F). To further support expression of TMEM16F in motoneurons, we performed co-staining with the pre-synaptic marker Synaptophysin. We observed that TMEM16F labeling appears on the opposite side of Synaptophysin, without any close apposition (Figure 2G). Interestingly, co-staining with Synaptobrevin (VAMP2) shows that TMEM16F cluster is closely facing the largest clusters of VAMP2, which are considered to be C-boutons (Hellström et al., 1999) (Figure 2H). The pattern of TMEM16F expression together with its close apposition with VAMP2 suggests a specialized function in association with the synaptic machinery. This led us to investigate the identity of the pre-synaptic

(F) Illustration of tail currents elicited at different voltages following activation of voltage-gated Ca2+ current under isotonic 140 mM $[Cl^-]$ and (H) mean current-voltage relationships of tail amplitude showing that the tail current reversal potential (E_{rev}) is around 0 mV (2.8 ± 0.8 mV) and the amplitude is significantly decreased in *Tmem16f*$^{-/-}$ motoneurons (* $p < 0.05$; ** $p < 0.01$, t-test).

(G) Illustration of tail currents under 10 mM $[Cl^-]_i$ and (I) mean current-voltage relationships of tail amplitude showing that setting $[Cl^-]_i$ at 10 mM induces a shift of E_{rev} toward negative potentials (−60.2 ± 1.6 mV), and the amplitude is significantly decreased in *Tmem16f*$^{-/-}$ motoneurons. Motoneuron numbers are indicated in brackets (t test). All values shown are means ± standard error of the mean (SEM) of three independent experiments (* $p < 0.05$; ** $p < 0.01$, t-test).

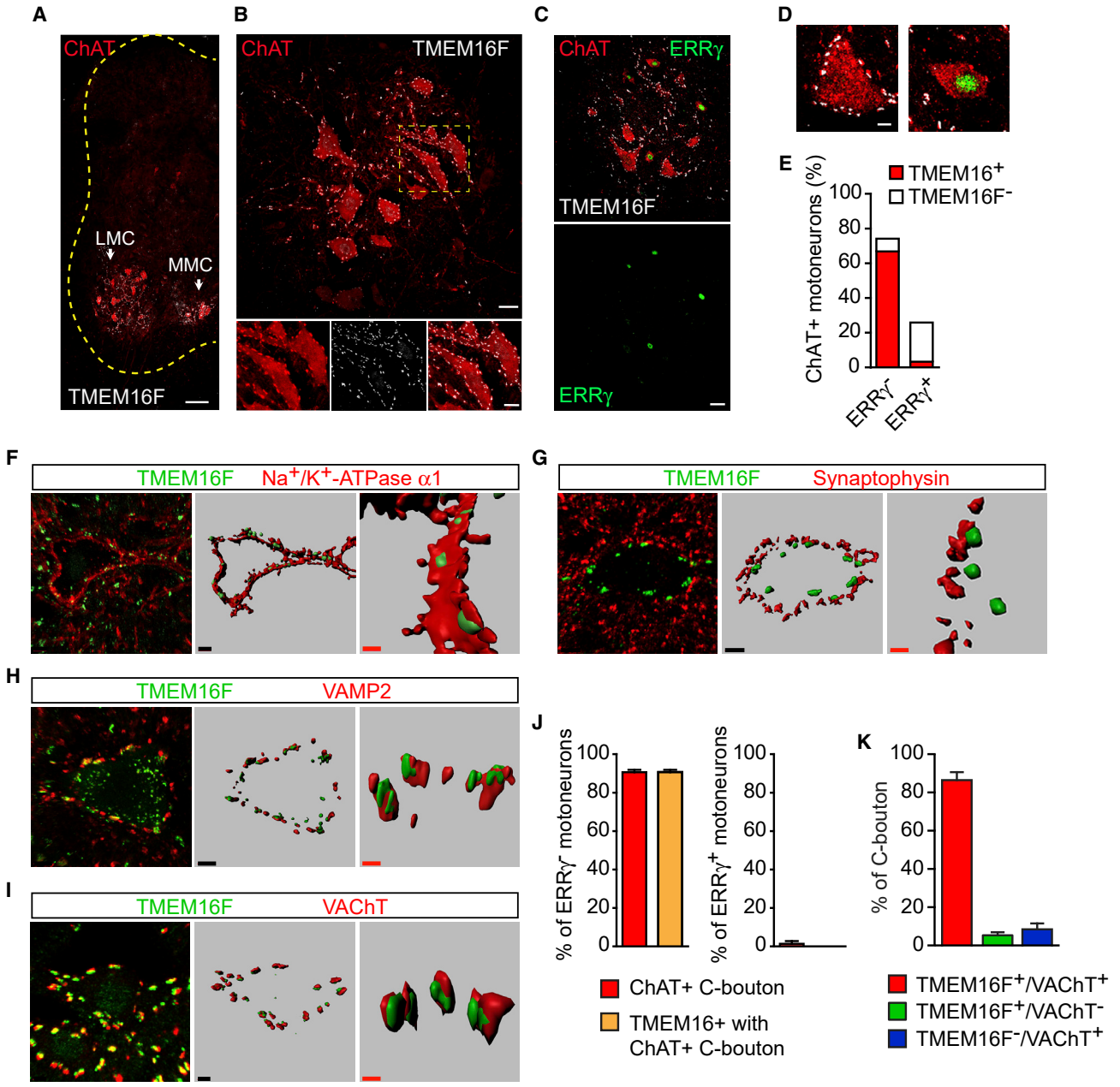

Figure 2. TMEM16F Is a α-Motoneuron Marker that Faces Cholinergic C-Bouton Synapses

(A) TMEM16F is expressed in cholinergic ChAT$^+$ motoneurons located in the lateral and medial motor columns (LMC and MMC, white arrow) of the spinal cord ventral horn. Scale bar, 100 μm.

(B) TMEM16F expression is clustered around soma and proximal dendrites of ChAT$^+$ motoneurons. High magnifications of the yellow-dashed box are shown on the panels below. Scale bar, 20 μm.

(C–D) Among ChAT$^+$ motoneurons, TMEM16F is almost exclusively expressed in ERRγ-negative (ERRγ$^-$) a-motoneurons compared to ERRγ-positive (ERRγ$^+$) g-motoneurons. Scale bar, 20 μm in (C) and 5 μm in (D).

(A)–(D) show representative confocal images of spinal cord sections of 2-month-old wild-type mice.

(E) Quantification of the number of ERRγ$^-$ and ERRγ$^+$ ChAT$^+$ neurons expressing or not TMEM16F (among the TMEM16F$^+$ motoneurons: 66.8% ± 4.9% are ERRγ$^-$ and 3.2% ± 1.9% are ERRγ$^+$; among the TMEM16F$^-$ motoneurons: 7.3% ± 1.0% are ERRγ$^-$ and 22.6% ± 2.3% ERRγ$^+$; n = 3 mice).

(F–I) Three-dimensional reconstruction of motoneurons (identified with SMI-32 staining, not shown) immunolabeled with TMEM16F and the Na$^+$/K$^+$-ATPase α1 subunit, a plasma membrane marker of α-motoneurons (F), the pre-synaptic markers, Synaptophysin (G), VAMP2 (H), and the pre-synaptic cholinergic marker VAChT (I). Binary images show that TMEM16F clusters are co-localized with the plasma membrane of motoneurons (F) and are distinct from pre-synaptic

(legend continued on next page)

neurotransmitter impinging on the TMEM16F clusters. Staining of glutamatergic synapses at the motoneuron soma using the vesicular glutamate transporter 1 (VGLUT1) revealed no specific co-localization with TMEM16F, while rare localization in front of the highly expressed VGLUT2 was observed (Figures S3A and S3B). The vesicular acetylcholine transporter (VAChT), a marker of synaptic cholinergic C-boutons, was characterized by a clustered expression at motoneuron soma and proximal dendrites. We observed that TMEM16F$^+$ clusters were facing VAChT$^+$ pre-synaptic clusters (Figure 2I). In agreement with previous studies (Deardorff et al., 2014), we observed that C-boutons are found predominantly in ERRγ^- α-motoneurons. Here, we found that approximately 90% of TMEM16F staining is observed in α-motoneurons (Figure 2J). Moreover, the vast majority of TMEM16F clusters are facing VAChT$^+$ clusters at C-boutons (Figure 2K). Collectively, these data establish that TMEM16F is a partner in the post-synaptic machinery of cholinergic C-boutons in α-motoneurons.

TMEM16F Controls Recruitment Threshold of Fast Motoneurons

We next investigated the effects of TMEM16F loss of function on electrical properties, by recording retrogradely Fluoro-gold-labeled motoneurons in lumbar spinal cord slices from post-natal day 7 (P7) to P11 mice. Passive properties defined by rheobase (RB) and input resistance (Rin) correctly predict motor-unit type (Zengel et al., 1985) and are used as biophysical hallmarks of α- and γ-motoneurons (Hadzipasic et al., 2014; Manuel and Heckman, 2011; Müller et al., 2014). Therefore, to discriminate between motoneuron subtypes, we analyzed the frequency distribution of Rin of wild-type (WT) and *Tmem16f*$^{-/-}$ motoneurons (Figure 3A). This distribution was best fitted with two Gaussian curves, which allowed identification of the slow (type 1) over the fast motoneuron population. According to Rin, the cutoff between the two populations was 90 MΩ. To further analyze the fast population, we plotted the frequency distribution of the RB of motoneurons with a Rin < 90 MΩ (Figure 3B). Fitting with two Gaussian curves allowed us to determine a cutoff value for RB between two fast motoneuron populations, type 2 and type 3, amounting to 450 pA. Analysis of the RB-Rin relationship showed a similar distribution of the different subtypes of motoneurons in WT and *Tmem16f*$^{-/-}$ mice, with the lower Rin necessitating the highest current amplitudes (Figures 3C and 3D). According to the frequency distribution analysis of Rin and RB, motoneurons in both genotypes could be classified into type 1, 2, and 3 populations (Figures 3C and 3D), which merely represents a biophysical continuum from the slow (type 1) to the FR (type 2) and FF (type 3) α-motoneurons. Despite comparable Rin, targeted exon ablation in *Tmem16f* significantly increased the RB of the type 3 population, while the trend to increased RB in type 2 motoneurons was not significant (Figures 3E and 3F). Analysis of membrane capacitance of type 3 population did not show any statistical differences between WT and *Tmem16f*$^{-/-}$ motoneurons (239 ± 23 pF, n = 14, and 295 ± 26 pF, n = 10, for type 3 WT and *Tmem16f*$^{-/-}$, respectively; ns, t test). Consistent with RB, the peak value of repolarization levels during repetitive activity was significantly more depolarized in type 3 *Tmem16f*$^{-/-}$ motoneurons (Figures 3G and 3H). In addition to enhanced depolarized voltage levels at a given current, the delay to spike initiation was significantly shorter in type 3 *Tmem16f*$^{-/-}$ motoneurons (Figures 3I and 3J), suggesting that TMEM16F contributes to the slow depolarization that characterizes the population of motoneurons with delayed firing (see Figure 3D for an example of delayed firing in type 2 and 3 versus immediate firing in type 1). Altogether, our data show that TMEM16F activation produces an outward current contributing to the recruitment threshold of the fast motoneuron population.

TMEM16F Controls Muscarinic Efficacy and Exercise Capacity

Active electrical properties are characterized by frequency-current (f-I) relationships; the gain is determined by calculating the slope of the f-I curve. The gain of the f-I curve in WT motoneurons was significantly higher in type 1 compared to type 2 and 3 populations (type 1, 73.5 ± 8.6 Hz nA^{-1}, n = 7; type 2, 41.1 ± 2.8 Hz nA^{-1}, n = 5, and type 3, 27.1 ± 1.7 Hz nA^{-}1, n = 14; ****p < 0.0001, one-way ANOVA with Tukey's post hoc test) (Figures 4A and 4B). While we observed that in *Tmem16f*$^{-/-}$ motoneurons, the gain of the f-I curve was also significantly higher in type 1 compared to the two other types (type 1, 60.9 ± 6.2 Hz nA^{-1}, n = 7; type 2, 35.9 ± 3.3 Hz nA^{-1}, n = 7; and type 3, 27.6 ± 1.4 Hz nA^{-1}, n = 10; ****p < 0.0001, one-way ANOVA with Tukey's post hoc test); we did not find any statistical difference between WT motoneurons and motoneurons with TMEM16F loss of function (Figure 4C). This result suggests that, contrary to K$^+$ channels, TMEM16F-CaCCs are not activated during electrical activity. As TMEM16F localized close to C-boutons, we examined whether it could influence the muscarinic modulation of the gain. We confirmed that oxotremorine, a muscarinic receptor agonist, induces an increase in motoneuron firing frequency (Miles et al., 2007), but analysis of its effects according to motoneuron type evidenced an order of efficacy from type 3 > type 2 >> type 1 (Figure 4D). The effects of oxotremorine on the gain were not modified in *Tmem16f*$^{-/-}$ motoneurons, but, as illustrated in Figures 4E and 4F, changing threshold recruitment strongly affected *de facto* the efficacy of muscarinic modulation of the firing frequency of the type 3 population at threshold and suprathreshold values. Plotting the mean f-I curves under control and in the presence of oxotremorine clearly evidences that the

Synaptophysin$^+$ vesicle clusters but are closely facing the pre-synaptic VAMP2 (H) and cholinergic VAChT$^+$ clusters at C-Boutons (I). High magnifications of representative spatial orientations are shown on the right panels. Scale bars, 5 μm (black) and 3 μm (red).

(J) Quantification of C-bouton-expressing neurons among muscle-contracting α-motoneurons (ERRγ^-) and γ-motoneurons (ERRγ^+ fusimotor population). 90% of α-motoneurons are contacted by ChAT$^+$ C-bouton synapses and show TMEM16F synaptic clusters, while the remaining 10% γ-motoneurons show negligible C-bouton synapses and do not express TMEM16F.

(K) Quantification of TMEM16F$^+$ synaptic clusters facing VAChT$^+$ C-boutons in motoneurons of the spinal cord of wild-type mice at 2 months of age. Results shown are the mean values ± SEM of at least three independent experiments.

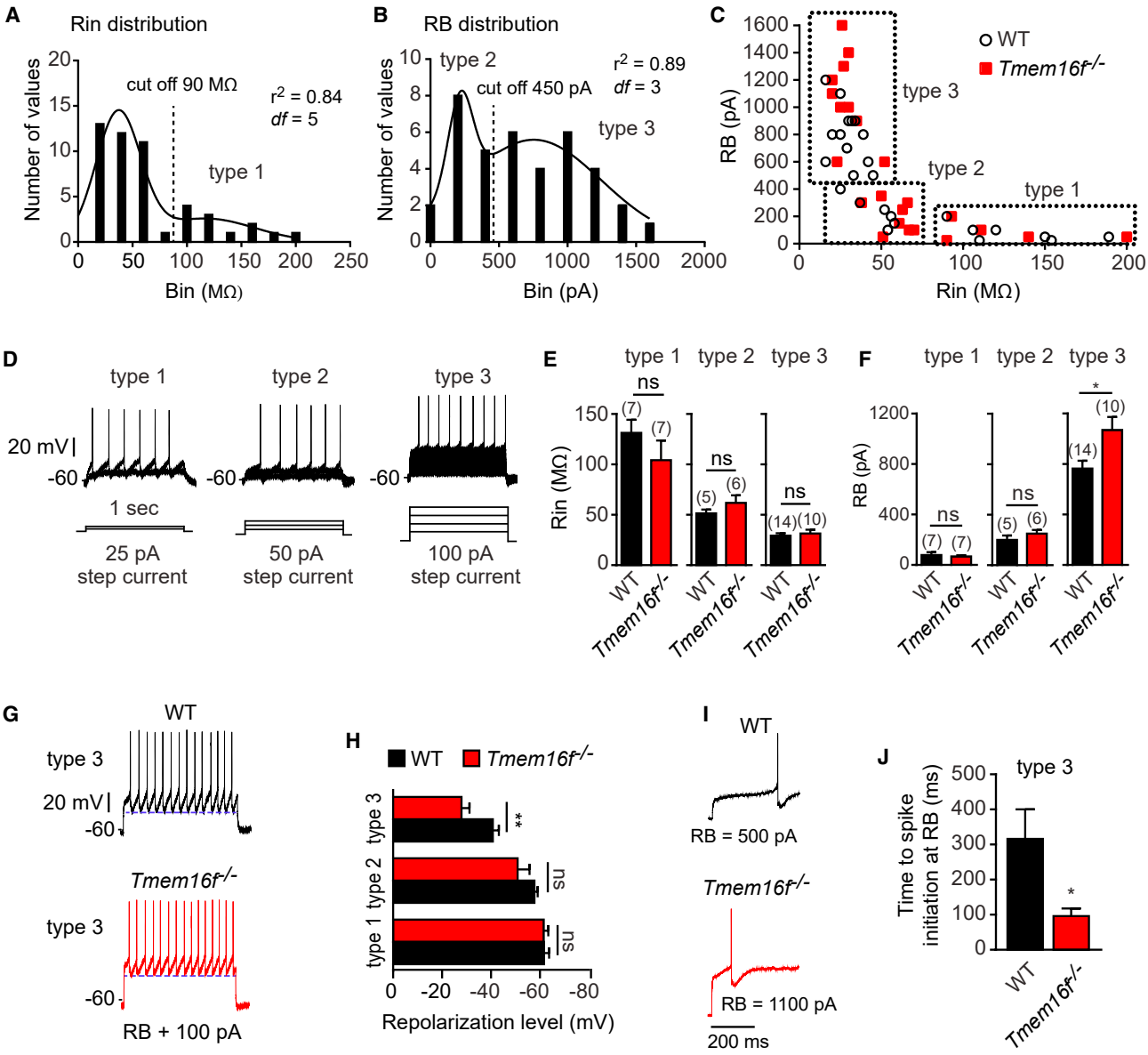

Figure 3. TMEM16F Controls Threshold Recruitment of Fast Motoneurons

(A) Histogram of frequency distribution of input resistance (Rin). Best fit is the sum of two Gaussian curves (bin center set at 20 MΩ; n = 49 motoneurons).

(B) Histogram of frequency distribution of threshold current (rheobase [RB]). Best fit is the sum of two Gaussian curves (bin center set at 200 pA; n = 38 motoneurons).

(C) Plots of RB versus Rin show similar distributions between 26 WT and 23 *Tmem16f*$^{-/-}$ motoneurons (recorded from at least five pups for each genotype). The type 1, type 2, and type 3 motoneuron populations are delineated according to the cut-off determined previously (A and B).

(D) Current-clamp recordings of electrical activity of Fluoro-gold-labeled motoneurons from post-natal day 7 (P7) to P11 mouse spinal cord. Representative examples of RB needed to elicit electrical activity using 1-s depolarization are shown.

(E) Rin is comparable between WT and *Tmem16f*$^{-/-}$ motoneurons for each of the three motoneuron subtypes (ns, not significant, t-test).

(F) Analysis of RB among the three WT and *Tmem16f*$^{-/-}$ motoneuron populations (* $p < 0.05$; ns, not significant, t-test).

(G) Typical firing of type 3 WT and *Tmem16f*$^{-/-}$ motoneurons during 1-s depolarization at RB +100 pA.

(H) The peak repolarization measured at RB + 1 step current (25 pA for type 1; 50 pA for type 2; and 100 pA for type 3) is more depolarized in type 3 *Tmem16f*$^{-/-}$motoneurons. (E, F, and H) Type 1: n = 7 and n = 7; type 2: n = 5 and n = 6; type 3: n = 14 and n = 10, WT and *Tmem16f*$^{-/-}$ motoneurons, respectively. Values are means ± SEM; *$p < 0.05$; **$p < 0.01$; ns, non-significant, t test.

(I) Representative voltage traces showing the short latency to fire of *Tmem16f*$^{-/-}$ motoneurons compared to WT, during 1-s depolarization at RB.

(J) Time to first spike initiation at RB is significantly decreased in type 3 *Tmem16f*$^{-/-}$ motoneurons. Values are means ± SEM; n = 14 and n = 10, WT and *Tmem16f*$^{-/-}$ motoneurons, respectively; t test.

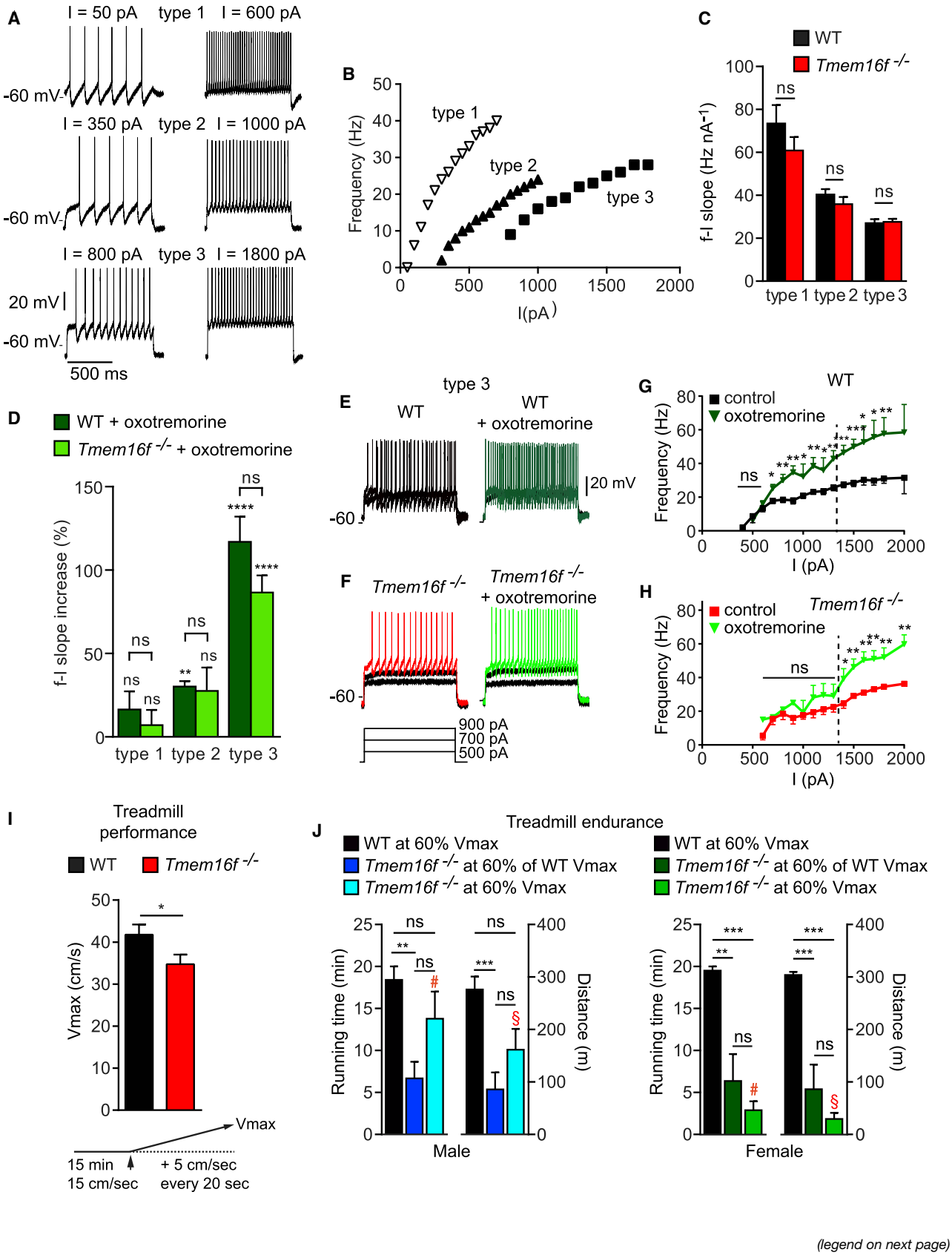

(legend on next page)

increase in firing frequency is significant from 700-pA current injection in WT motoneurons, while in *Tmem16f*$^{-/-}$ motoneurons the significance is reached from 1,400 pA (Figures 4G and 4H). Altogether, these data demonstrate that, despite the absence of direct muscarinic activation of TMEM16F-dependent outward current, the shift in threshold recruitment is sufficient to induce an overall decrease in neuromodulation.

We next sought to determine the functional outcome of TMEM16F loss of function on motor tasks. Locomotor pattern and task-dependent behaviors were assessed in 2-month-old WT and *Tmem16f*$^{-/-}$ mice. We did not observe any significant differences between WT and *Tmem16f*$^{-/-}$ mice in the maximum walking speed during spontaneous activity with the open field test, or in the pattern of right-left alternation using the Catwalk assay, or on muscle strength as determined with the grid test (Figures S4A–S4C). These results suggest that TMEM16F is not involved in walking, movement coordination, or muscle strength development. In contrast, evaluation of motor performance with the treadmill exhaustion test revealed a significant 17% decrease in the maximal running speed in *Tmem16f*$^{-/-}$ mice (Figure 4I). We did not observe any significant differences between male and female mice (not shown). For endurance assessment, the treadmill speed was first set at 60% of the WT maximal speed. Data analyses showed that, at this high speed, both male and female *Tmem16f*$^{-/-}$ mice were unable to run as far or for as long as control littermates (Figure 4J). However, setting the speed at 60% of their own V_{max} revealed that male *Tmem16f*$^{-/-}$ mice performed better that female *Tmem16f*$^{-/-}$ mice, which evidences a sex-dependent effect of *Tmem16f* deletion on endurance (Figure 4J). Hence, by controlling recruitment of fast motoneurons, TMEM16F impacts muscarinic modulation and exercise with high levels of task demand.

Loss of TMEM16F Function Reduces ALS Progression in Male SOD1^{G93A} Mice

To investigate the role of TMEM16F in ALS, a neurodegenerative disease that preferentially impairs the function of fast α-motoneurons, we bred *Tmem16f*$^{-/-}$ mice with *SOD1*^{G93A} mice, a well-characterized and rapidly progressive model of ALS (Bowerman et al., 2015; Gurney et al., 1994). Analysis of weight curves of male and female mice revealed no significant effects of *Tmem16f* exon deletion under physiological conditions (Figures S5A and S5B). However, the disease onset, defined as the age that peak weight was reached (Aebischer et al., 2011), was significantly delayed in *SOD1*^{G93A}*; Tmem16*$^{-/-}$ male but not in *SOD1*^{G93A}*; Tmem16*$^{-/-}$ female mice (Figure 5A) compared to *SOD1*^{G93A} mice of the corresponding sex. This was further confirmed by defining disease onset to reduction of motor performance in grid test (Figures S5C–S5E). Interestingly, TMEM16F loss of function did not significantly extended the life span of both male and female *SOD1*^{G93A} mice (Figure 5B). We next determined the motor decline of *SOD1*^{G93A}*; Tmem16f*$^{-/-}$ and *SOD1*^{G93A} mice and observed that the progressive deterioration of muscle strength was significantly retarded in *SOD1*^{G93A}*; Tmem16*$^{-/-}$ male, but not in *SOD1*^{G93A}*; Tmem16*$^{-/-}$ female mice, compared to sex-matched *SOD1*^{G93A} mice (Figures 5C and 5D).

Motoneuron survival was then assessed at 110 and 130 days of age. In the context of ALS, the total number of ChAT^{+} motoneurons significantly decreased in *SOD1*^{G93A} and *SOD1*^{G93A}*;Tmem16f*$^{-/-}$ mice at both ages compared to age-matched WT mice. However, we did not observe any significant differences between *SOD1*^{G93A}*;Tmem16f*$^{-/-}$ male and female mice at both 110 and 130 days of age (Figures S6A and S6B). More in-depth analysis of motoneuron degeneration using matrix metalloproteinase 9 (MMP9), a selective marker of vulnerable motoneurons (Kaplan et al., 2014), revealed a significant decrease in motoneuron survival in both male and female ALS mice, which was not significantly affected by TMEM16F loss of function (Figures S6C and S6D).

In ALS mice, motoneuron stress is detected prior to death and correlates with denervation (Pun et al., 2006). Therefore, we determined the expression of activating transcription factor 3 (ATF3), an activity-regulated inhibitor of death gene, used as a marker of early stress marker in vulnerable motoneurons (Saxena et al., 2009; Zhang et al., 2009) and the innervation of the neuromuscular junction. Targeted exon deletion in *Tmem16f* in

Figure 4. TMEM16F Contributes to Muscarinic Modulation and to Exercise-Dependent Locomotor Activity

(A) Representative traces of action potentials evoked by injected currents (I, pA) in types 1, 2, and 3 motoneurons. Liminal (left) and supraliminal (right) depolarizing pulses are shown.

(B) Frequency-current (f–I) relationships of the three subtypes of motoneurons.

(C) Mean slopes of the f–I curves do not differ between WT and *Tmem16f*$^{-/-}$ motoneurons (type 1: n = 7 and n = 7; type 2: n = 5 and n = 6; type 3: n = 14 and n = 10, WT and *Tmem16f*$^{-/-}$ motoneurons, respectively; ns, not significant, t test).

(D) Superfusion with 10 μM oxotremorine increases the gain of firing frequency, determined with the slope of f–I relationships (16.4% ± 10.9%, n = 5, and 7.0% ± 9.2%, n = 6 for type 1; 30.2% ± 3.3%, n = 4, and 27.0% ± 13.6%, n = 7 for type 2; and 116.9% ± 15.1%, n = 7, and 86.6% ± 10.2%, n = 10, for type 3, in WT and *Tmem16f*$^{-/-}$ motoneurons, respectively). Values are means ± SEM; **p < 0.01, ****p < 0.0001, paired t test for each genotype and unpaired t test between genotypes.

(E and F) Illustration of oxotremorine effect in type 3 populations at similar depolarizing pulses in WT (E) and *Tmem16f*$^{-/-}$ (F) motoneurons.

(G and H) Plot of the mean f–I curves of the type 3 population in the presence, or not (control), of 10 μM oxotremorine. The dashed line evidences the rightward shift in muscarinic modulation between WT (G) and *Tmem16f*$^{-/-}$ (H) motoneurons. Values are means ± SEM; *p < 0.05, ***p < 0.001, t test.

(I and J) Assessment of exercise capacity using a 10°-inclined treadmill.

(I) Evaluation of motor performance in WT and *Tmem16f*$^{-/-}$ mice by treadmill exhaustion. The maximal speed, V_{max}, was 41.7 ± 2.4 and 34.7 ± 2.2 cm/s in 17 WT and 19 *Tmem16f*$^{-/-}$ mice, t test; protocol is shown below the graph and V_{max} is the fastest speed at which mice can run (* p < 0.05, t-test).

(J) Endurance capacity of WT and *Tmem16f*$^{-/-}$ mice was determined by treadmill test. When a 20-min running time is imposed at 60% of their V_{max}, WT male and female can perform the imposed time covering a similar distance (18.4 ± 1.6 min and 276 ± 24 m, n = 10, and 19.5 ± 0.5 min and 304 ± 6 m, n = 7, for male and female, respectively). The running time and the distance at 60% of WT V_{max} were 6.7 ± 2.0 min and 86 ± 32 m, n = 10, and 6.4 ± 3.2 min and 86 ± 47 m, n = 7, for male and female *Tmem16f*$^{-/-}$ mice, respectively. At 60% of *Tmem16f*$^{-/-}$ V_{max}, the running time and distance were 13.8 ± 3.2 min and 162 ± 40 m, n = 7, and 2.9 ± 1.1 min and 29 ± 12 m, n = 4, for male and female *Tmem16f*$^{-/-}$ mice, respectively. Values are means ± SEM; $^{\#}$p < 0.05 *Tmem16f*$^{-/-}$ male versus *Tmem16f*$^{-/-}$ *female* at 60% V_{max} for running time and §p < 0.05 *Tmem16f*$^{-/-}$ male versus *Tmem16f*$^{-/-}$ *female* at 60% V_{max} for distance, one-way ANOVA with Tukey's post hoc test.

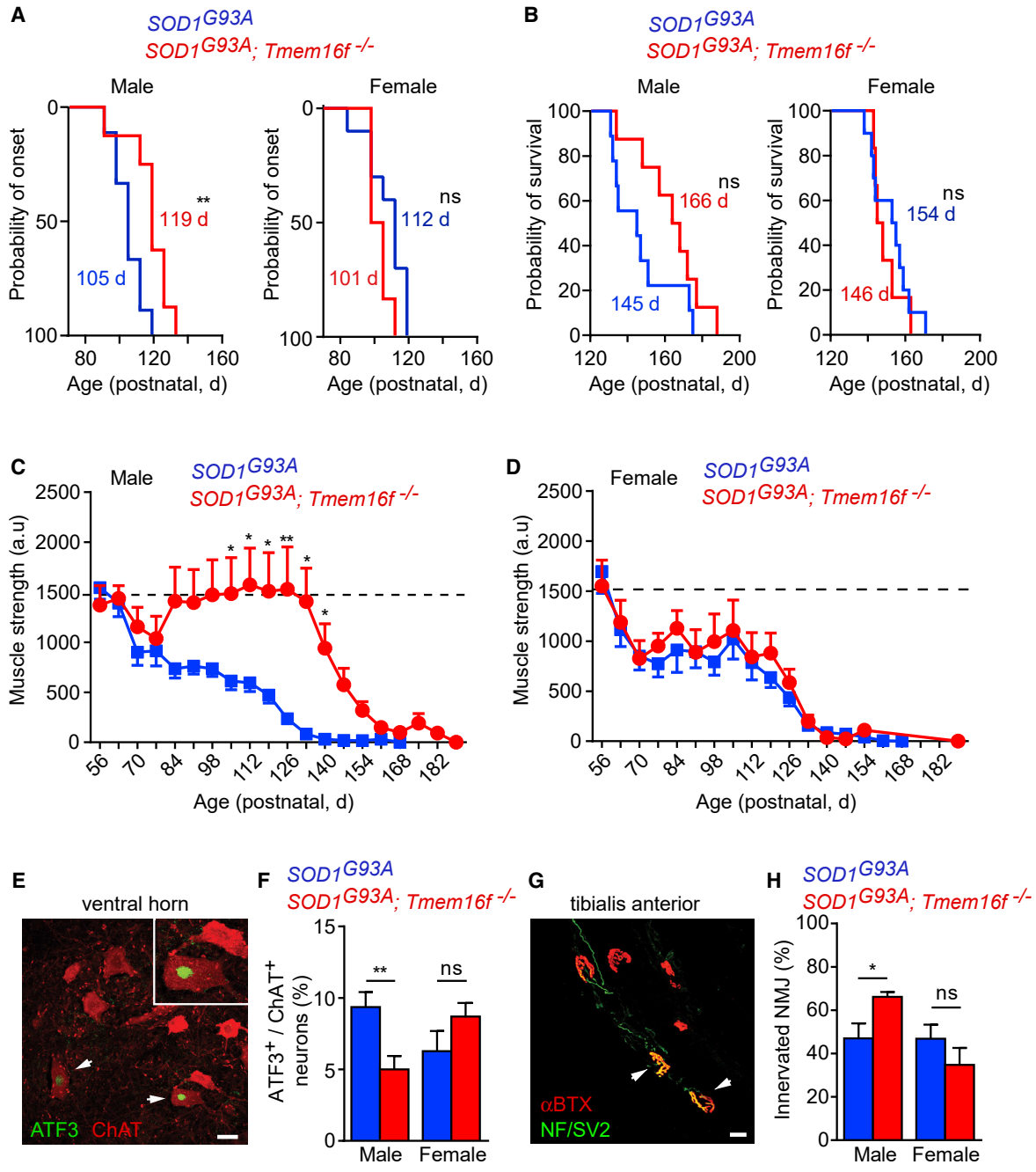

Figure 5. Targeted Exon Deletion in *Tmem16f* Delays Disease Onset, Improves Motor Performance of Male SOD1^{G93A} Mice, and Protects Motoneurons from Stress

(A) Probability of onset was determined by the peak of the body weight curve of male and female *SOD1^{G93A}* and *SOD1^{G93A}; Tmem16f$^{-/-}$* mice.

(B) Kaplan-Meier survival curves for male and female *SOD1^{G93A}* and *SOD1^{G93A}; Tmem16f$^{-/-}$* mice. (A and B) The median age in days (d) is indicated, n = 9 male and n = 10 female *SOD1^{G93A}* mice; n = 8 male and n = 6 female *SOD1^{G93A}; Tmem16f$^{-/-}$* mice; **p < 0.01, Log-rank test.

(C and D) Muscle strength of male (C) and female (D) *SOD1^{G93A}* and *SOD1^{G93A}; Tmem16f$^{-/-}$* mice was evaluated weekly starting at 56 days of age by grid test (arbitrary unit [a.u.]). Values are expressed as mean ± SEM, same cohorts of mice as in (A); *p < 0.05, two-way repeated-measure ANOVA with the Newman-Keuls post hoc test.

(E) Representative immunostaining showing ChAT^{+} motoneurons expressing the ATF3 stress marker in the spinal cord of *SOD1^{G93A}* mice at 110 days of age. Scale bar, 20 μm.

(F) Quantification of ATF3/ChAT double-positive motoneurons per lumbar ventral horn hemisection in the spinal cord of 110-day-old male and female *SOD1^{G93A}* and *SOD1^{G93A}; Tmem16f$^{-/-}$* mice. Values are means ± SEM, n = 14 sections, from three mice for each genotype, t test.

(legend continued on next page)

SOD1^{G93A} mice induced a significant decrease in the number of ATF3-positive motoneurons (Figures 5E and 5F) and correlated with reduced denervation of the fast-twitch tibialis anterior muscle in *SOD1*^{G93A}*; Tmem16f*$^{-/-}$ male, but not in female mice compared to *SOD1*^{G93A} mice (Figures 5G and 5H). Therefore, the loss of TMEM16F function protects motoneurons from activity-dependent early stress and delays disease onset, only in male mice.

DISCUSSION

We found that TMEM16F is selectively expressed in spinal motoneurons and under physiological conditions contributes to the expression of an outwardly rectifying Ca^{2+}-activated Cl^- current. It is noteworthy that *Tmem16b* is also enriched in motoneurons, which made it a good candidate for motoneuronal CaCC (Zhang et al., 2017). However, the use of *Tmem16f*$^{-/-}$ mice together with the single-cell RNA interference support a major role of *Tmem16f*$^{-/-}$ in CaCCs expressed in motoneurons. Discrepancies exist concerning the ionic permeability of TMEM16F, as it has been described as a non-specific cation channel, a chloride channel, and a mixed cationic/chloride channel (Kunzelmann et al., 2014; Picollo et al., 2015). Here, we show that in HEK293T cells, activation of mouse TMEM16F induces an outwardly rectifying current whose reversal potential is consistent with a predominant Cl^- permeability over cations. Cell-type-specific features as well as ionic environment could account for such variability. Moreover, the source of Ca^{2+} is a key factor for Ca^{2+}-activated Cl^- conductance activation. In sensory neurons, voltage-dependent Ca^{2+} currents are more efficient than ionomycin at activating Best1-Cl^- conductance (Boudes et al., 2009), while inositol 1,4,5-triphosphate-induced Ca^{2+} mobilization is necessary for pain related to TMEM16A-CaCC activity (Liu et al., 2010). We also observed that ionomycin does not activate a Cl^- current in motoneurons (not shown). Altogether, these data could account for the discrepancies concerning the ionic nature of TMEM16F, but also shed more light on the molecular complexity of this protein family.

Identification of different recruitment thresholds has led to the identification of three main subpopulations of adult α-motoneurons *in vivo* (Burke et al., 1973; Gustafsson and Pinter, 1984). Here, using the same electrophysiological criteria, i.e., input resistance and rheobase, we defined three subpopulations of motoneurons recorded from mice post-natal spinal cord slices. To our knowledge, two recent studies also differentiate motoneuron sub-types in post-natal mouse motoneurons based on electrophysiological properties, morphological, and molecular markers. In the first study, based on the identification of a gene associated with a fast motor pool, the authors identified low-input resistance/high-rheobase motoneurons from the slow motoneuron population (Müller et al., 2014). Their classification supports that type 2 and 3 motoneuron subtypes are fast motoneurons and type 1 belongs to the slow motoneuron. The study of Zytnicki's group (Leroy et al., 2014) provides additional information for defining motoneuron sub-types. Combining electrophysiological measurements with immunostainings with ERRβ, a marker of the slow motoneuron population, they show that slow motoneurons have the lowest excitability threshold and an immediate firing with long pulse duration, which fits with electrophysiological properties of type 1 population. The ERRβ-negative fast motoneurons have a delayed firing and a higher rheobase, which is also consistent with the electrophysiological hallmark of type 2 and 3 motoneurons (see Figures 3D and 3I). Quite interestingly, their study also provides data supporting a sub-classification of the fast motoneurons into chondrolectin (Chodl)-positive and Chodl-negative motoneurons. The Chodl-positive have the highest rheobase and could correspond to the type 3 population, and the Chodl-negative have a lower rheobase and could correspond to the type 2 population. Altogether, these data strongly support the proposal to classify of neonatal mouse motoneurons into three subtypes based on biophysical properties, which might be representative of S, FR, and FF motoneurons.

We found that TMEM16F is merely involved in the rheobase of type 3 and, to a lesser extent, type 2 motoneurons. Interestingly, it has been demonstrated that slow subthreshold membrane depolarization observed at high rheobase and long pulse duration is responsible for the delayed firing of fast motoneurons. Progressive inhibition or activation of voltage-dependent conductance is involved in the slow subthreshold membrane depolarization (Bos et al., 2018; Leroy et al., 2015). Here, under low intracellular Ca^{2+} buffering (0.1 mM EGTA), we show that at high rheobase, the outward CaCC does also contribute to the subthreshold membrane depolarization. As we previously showed (Hilaire et al., 2005), kinetics of voltage-gated Ca^{2+} channels and intracellular Ca^{2+} buffering control activation and inactivation of CaCC. We propose that progressive decrease in intracellular Ca^{2+} during long pulse duration leads to the inactivation of CaCC. In *Tmem16f*$^{-/-}$ motoneurons, the absence of outward current induces a higher level of membrane depolarization together with a faster "slow depolarization" responsible for firing recruitment. The lack of effect on firing properties of motoneurons demonstrates that, contrary to K^+ channels (see, for review, Brownstone, 2006), TMEM16F impacts only the recruitment of delayed firing motoneurons, but not firing frequency. This strongly supports the point that TMEM16F-CaCC is minimally activated compared with K^+ channels during an action potential.

By facing C-boutons, TMEM16F might contribute to the cholinergic regulation of motoneurons during task-dependent modulation (Zagoraiou et al., 2009). Task-dependent demand involves the recruitment of FR and FF motoneurons, which, according to our classification, corresponds to type 2 and 3 motoneurons, respectively. Remarkably, we show that the population with the highest RB is the most impacted by both muscarinic

(G) Representative image of innervated (white arrows) and denervated motor endplates in tibialis anterior muscle of 110-day-old *SOD1*^{G93A} identified by staining of the post-synaptic apparatus with α-bungarotoxin (αBTX, red) and axons with neurofilament (NF)/synaptic vesicle glycoprotein 2A (SV2) antibodies (in green). Scale bar, 20 μm.

(H) The percentage of fully innervated neuromuscular junction (NMJ) was determined in tibialis anterior muscle of male and female *SOD1*^{G93A} and *SOD1*^{G93A}; *Tmem16f*$^{-/-}$ mice at 110 days of age. Values are means ± SEM; four muscles from four mice for each genotype; *$p < 0.05$, t test.

regulation and the loss of TMEM16F function. Cholinergic neuromodulation is reported to increase firing frequency by inhibiting Ca^{2+}-activated K^+ channels (Miles et al., 2007). Interestingly, we show a 30% ± 3% increase of firing frequency in type 2 motoneuron, a value similar to the one reported by Miles et al. (2007) (35% ± 8% increase at a 200-pA rheobase). For type 3 populations, the 117% ± 15% increase is also observed when inhibiting SK current with apamin and interestingly at high rheobase (600 pA and 116% increase in firing frequency). Concerning type 1, the variability did not allow reaching significance probably due to the mixed slow motoneuron and γ-motoneuron. These data strongly support the motoneuron type-dependent effects of oxotremorine, which are most probably related to the recruitment of SK channels. Here, we show that modulation of threshold recruitment confers to TMEM16F the ability to modify the impact of the neuromodulation at a given input. In addition, when we analyzed the muscarinic regulation of firing frequency according to our classification, we evidence that Ca^{2+}-activated K^+ and Cl^- channel activities converge to regulate type 3 motoneuron excitability. Both channels generate outward currents whose functional contribution is dependent on their driving force, which explains a similar voltage responsiveness toward type 3 motoneurons. Consistent with morphological and electrophysiological data, we reveal a role for TMEM16F in forced exercise on an inclined treadmill, while no significant effects were noted during spontaneous walking. Forced exercise, assessed by V_{max} measurement and also by endurance testing of *Tmem16f*$^{-/-}$ mice at 60% of WT V_{max}, involves the recruitment of high-RB type 3 motoneurons (potentially FF motoneurons) and neuromodulation of their activity, which is consistent with the effects of TMEM16F on the excitability threshold. Using a moderate exercise at 60% of *Tmem16f*$^{-/-}$ V_{max} relies mainly on the recruitment of aerobic metabolism that involves FR fibers. At 60% of *Tmem16f*$^{-/-}$ V_{max}, no significant differences were observed between *Tmem16f*$^{-/-}$ male mice compared with WT, which is in agreement with the moderate effect of targeted exon deletion in *Tmem16f* on type 2 motoneurons. The lack of recovery in *Tmem16f*$^{-/-}$ females at 60% of their V_{max} suggests that, at an equivalent workload, they have to produce more effort than male mice and continue to recruit the high-threshold type 3 motoneurons. Such intrinsic sex differences could be related to muscle mass, which is an endurance predictor.

The role of motoneuron excitability in ALS remains under debate (Leroy et al., 2014; Martínez-Silva et al., 2018; Saxena et al., 2013). Here, we show that a targeted deletion in *Tmem16f* protects against the early insults that lead to loss of muscle strength. The cellular mechanisms by which loss of TMEM16F function preserves muscle strength are attributable to a reduced denervation, not to intrinsic performance. ALS motoneurons with targeted exon ablation in *Tmem16f* display a decreased ATF3 expression. This nuclear factor belongs to the set of activity-dependent genes upregulated following a large increase in $[Ca^{2+}]_i$ (Zhang et al., 2009). A salient characteristic of motoneurons is their high vulnerability to intracellular Ca^{2+} overload (Bernard-Marissal et al., 2012; Van Den Bosch et al., 2006), which is due to their low Ca^{2+} buffering capacity (von Lewinski and Keller, 2005). In ALS, increased levels of glutamate and expression of Ca^{2+}-permeable aminomethylphosphonic acid (AMPA) receptors contribute to Ca^{2+} overload and excitotoxicity (Grosskreutz et al., 2010). Accordingly, an increase in Ca^{2+}-activated Cl^- current amplitude could promote more excitability by decreasing the recruitment threshold of motoneurons, thereby further enhancing Ca^{2+} load. The decrease in ATF3 expression indicates that TMEM16F loss of function plays a role in protecting against activity-dependent Ca^{2+} overload. Therefore, our results demonstrate that the increase in excitability threshold of motoneurons protects against the Ca^{2+} overload that could occur during ionotropic and metabotropic synaptic stimulation.

The observation of sex-dependent effects of TMEM16F deletion in an ALS context is puzzling. Our data on the physiological role of TMEM16F indicate that the protein is functional in both sexes, as both male and female *Tmem16f*$^{-/-}$ mice displayed decreased performances. Therefore, specific sex-dependent expression of this protein is unlikely. However, the observation that females recover less effectively than males from endurance could contribute to the phenotype observed in ALS context. It is possible that, in females, the higher excitability toward an equivalent demand prevents reaching a cutoff level for protection. In support of this hypothesis, it is well established that there are fundamental differences in signaling pathways and plasticity between males and females (Herron and Miles, 2012; Jain et al., 2019) and a sex bias toward males has also been reported in a young population with ALS (McCombe and Henderson, 2010). Sex-specific regulation of the synaptic network and Ca^{2+} homeostasis in an ALS context is beyond the present study and will need further investigation.

By identifying TMEM16F as a post-synaptic component of C-boutons in motoneurons, our study emphasizes the need to identify the ionic channels involved in the recruitment threshold of motoneurons, as they determine not only the intrinsic level of excitability but also the level of neuromodulatory influence. In addition, this study strongly supports a role for excitatory networks in the development of motoneuron disease in an ALS context and to the potential of ionic channels as therapeutic candidates.

STAR★METHODS

Detailed methods are provided in the online version of this paper and include the following:

- KEY RESOURCES TABLE
- LEAD CONTACT AND MATERIALS AVAILABILITY
- EXPERIMENTAL MODEL AND SUBJECT DETAILS
  - Animals
  - Cell Line
- METHOD DETAILS
  - Motoneuron culture
  - Spinal cord slice preparation
  - Electrophysiological recordings
  - RNA extraction and RT-qPCR
  - RNA interference Experiments
  - Sequencing
  - TMEM16F expression vector and transfection
  - Immunohistochemistry
  - Functional tests

- QUANTIFICATION AND STATISTICAL ANALYSIS
- DATA AND CODE AVAILABILITY

SUPPLEMENTAL INFORMATION

Supplemental Information can be found online at https://doi.org/10.1016/j.celrep.2020.02.001.

ACKNOWLEDGMENTS

We thank Dr. Lily Yeh Yan for the generous gift of *Tmem16f*$^{-/-}$ mice and N-Ter anti-TMEM16F antibodies, Dr. Karl Kunzelmann for the generous gift of C-Term anti-TMEM16F antibodies, Dr. Pierre-François Mery for his help in slice preparation, Dr. Hassan Boukhaddaoui for 3D image reconstruction, Dr. Jérôme Bourien for his help in the analysis of frequency distribution, and Mr. Boris Tremblier for his help in preliminary experiments. We are grateful to the personnel of the Réseau d'Histologie Expérimentale de Montpellier, the MRI imaging facility, and the INM animal core facility. This work was supported by the Association Française contre les Myopathies (AFM) (17118 and 19496 to F.S.); Association pour la Recherche sur la Sclérose Latérale Amyotrophique (ARSLA) (to F.S.); Institut National de la Santé et Recherche Médicale (to C.R.); and ANR Mimetic (ANR-15-CE18-0017-01 to F.S. and ANR-14-RARE-0006 to C.R.). C. Soulard was supported by Ministère de l'Enseignement Supérieur de la Recherche et de l'Innovation and by ARSLA (PhD fellowship), and C. Salsac by ANR-14-RARE-0006.

AUTHOR CONTRIBUTIONS

Conceptualization, C.R. and F.S.; Investigation, C. Soulard, C. Salsac, K.M., C.H., J.R., A.M., and F.S.; Analysis, C. Soulard, K.M., S.L., C.R., and F.S.; Writing – Original Draft, F.S.; Writing – Review & Editing, C.R. and F.S.; Funding Acquisition, C.R. and F.S.; Supervision, C.R. and F.S.

DECLARATION OF INTERESTS

Authors declare no competing interests.

Received: July 13, 2019
Revised: November 12, 2019
Accepted: January 31, 2020
Published: February 25, 2020

REFERENCES

Aebischer, J., Cassina, P., Otsmane, B., Moumen, A., Seilhean, D., Meininger, V., Barbeito, L., Pettmann, B., and Raoul, C. (2011). IFNγ triggers a LIGHT-dependent selective death of motoneurons contributing to the non-cell-autonomous effects of mutant SOD1. Cell Death Differ. *18*, 754–768.

Arce, V., Garces, A., de Bovis, B., Filippi, P., Henderson, C., Pettmann, B., and deLapeyriere, O. (1999). Cardiotrophin-1 requires LIFRbeta to promote survival of mouse motoneurons purified by a novel technique. J Neurosci Res *55*, 119–126.

Bernard-Marissal, N., Moumen, A., Sunyach, C., Pellegrino, C., Dudley, K., Henderson, C.E., Raoul, C., and Pettmann, B. (2012). Reduced calreticulin levels link endoplasmic reticulum stress and Fas-triggered cell death in motoneurons vulnerable to ALS. J. Neurosci. *32*, 4901–4912.

Bos, R., Harris-Warrick, R.M., Brocard, C., Demianenko, L.E., Manuel, M., Zytnicki, D., Korogod, S.M., and Brocard, F. (2018). Kv1.2 channels promote nonlinear spiking motoneurons for powering up locomotion. Cell Rep. *22*, 3315–3327.

Boudes, M., Pieraut, S., Valmier, J., Carroll, P., and Scamps, F. (2008). Single-cell electroporation of adult sensory neurons for gene screening with RNA interference mechanism. J. Neurosci. Methods *170*, 204–211.

Boudes, M., Sar, C., Menigoz, A., Hilaire, C., Péquignot, M.O., Kozlenkov, A., Marmorstein, A., Carroll, P., Valmier, J., and Scamps, F. (2009). Best1 is a gene regulated by nerve injury and required for Ca^{2+}-activated Cl^- current expression in axotomized sensory neurons. J. Neurosci. *29*, 10063–10071.

Bowerman, M., Salsac, C., Coque, E., Eiselt, É., Deschaumes, R.G., Brodovitch, A., Burkly, L.C., Scamps, F., and Raoul, C. (2015). Tweak regulates astrogliosis, microgliosis and skeletal muscle atrophy in a mouse model of amyotrophic lateral sclerosis. Hum. Mol. Genet. *24*, 3440–3456.

Bowerman, M., Salsac, C., Bernard, V., Soulard, C., Dionne, A., Coque, E., Benlefki, S., Hince, P., Dion, P.A., Butler-Browne, G., et al. (2017). KCC3 loss-of-function contributes to Andermann syndrome by inducing activity-dependent neuromuscular junction defects. Neurobiol. Dis. *106*, 35–48.

Brownstone, R.M. (2006). Beginning at the end: repetitive firing properties in the final common pathway. Prog. Neurobiol. *78*, 156–172.

Burke, R.E., Levine, D.N., Tsairis, P., and Zajac, F.E., 3rd. (1973). Physiological types and histochemical profiles in motor units of the cat gastrocnemius. J. Physiol. *234*, 723–748.

Caputo, A., Caci, E., Ferrera, L., Pedemonte, N., Barsanti, C., Sondo, E., Pfeffer, U., Ravazzolo, R., Zegarra-Moran, O., and Galietta, L.J. (2008). TMEM16A, a membrane protein associated with calcium-dependent chloride channel activity. Science *322*, 590–594.

Cho, H., Yang, Y.D., Lee, J., Lee, B., Kim, T., Jang, Y., Back, S.K., Na, H.S., Harfe, B.D., Wang, F., et al. (2012). The calcium-activated chloride channel anoctamin 1 acts as a heat sensor in nociceptive neurons. Nat. Neurosci. *15*, 1015–1021.

de Carvalho, M., Eisen, A., Krieger, C., and Swash, M. (2014). Motoneuron firing in amyotrophic lateral sclerosis (ALS). Front. Hum. Neurosci. *8*, 719.

Deardorff, A.S., Romer, S.H., Sonner, P.M., and Fyffe, R.E. (2014). Swimming against the tide: investigations of the C-bouton synapse. Front Neural Circuits. https://doi.org/10.3389/fncir.2014.00106.

Delpy, A., Allain, A.E., Meyrand, P., and Branchereau, P. (2008). NKCC1 cotransporter inactivation underlies embryonic development of chloride-mediated inhibition in mouse spinal motoneuron. J Physiol. *586*, 1059–1075.

Edwards, I.J., Bruce, G., Lawrenson, C., Howe, L., Clapcote, S.J., Deuchars, S.A., and Deuchars, J. (2013). Na^+/K^+ ATPase α1 and α3 isoforms are differentially expressed in α- and γ-motoneurons. J. Neurosci. *33*, 9913–9919.

Grosskreutz, J., Van Den Bosch, L., and Keller, B.U. (2010). Calcium dysregulation in amyotrophic lateral sclerosis. Cell Calcium *47*, 165–174.

Gurney, M.E., Pu, H., Chiu, A.Y., Dal Canto, M.C., Polchow, C.Y., Alexander, D.D., Caliendo, J., Hentati, A., Kwon, Y.W., Deng, H.X., et al. (1994). Motor neuron degeneration in mice that express a human Cu,Zn superoxide dismutase mutation. Science *264*, 1772–1775.

Gustafsson, B., and Pinter, M.J. (1984). An investigation of threshold properties among cat spinal alpha-motoneurones. J. Physiol. *357*, 453–483.

Ha, G.E., Lee, J., Kwak, H., Song, K., Kwon, J., Jung, S.Y., Hong, J., Chang, G.E., Hwang, E.M., Shin, H.S., et al. (2016). The Ca^{2+}-activated chloride channel anoctamin-2 mediates spike-frequency adaptation and regulates sensory transmission in thalamocortical neurons. Nat. Commun. *7*, 13791.

Hadzipasic, M., Tahvildari, B., Nagy, M., Bian, M., Horwich, A.L., and McCormick, D.A. (2014). Selective degeneration of a physiological subtype of spinal motor neuron in mice with SOD1-linked ALS. Proc. Natl. Acad. Sci. USA *111*, 16883–16888.

Hartzell, H.C., Yu, K., Xiao, Q., Chien, L.T., and Qu, Z. (2009). Anoctamin/TMEM16 family members are Ca^{2+}-activated Cl^- channels. J. Physiol. *587*, 2127–2139.

Hellström, J., Arvidsson, U., Elde, R., Cullheim, S., and Meister, B. (1999). Differential expression of nerve terminal protein isoforms in VAChT-containing varicosities of the spinal cord ventral horn. J. Comp. Neurol. *411*, 578–590.

Herron, L.R., and Miles, G.B. (2012). Gender-specific perturbations in modulatory inputs to motoneurons in a mouse model of amyotrophic lateral sclerosis. Neuroscience *226*, 313–323.

Hilaire, C., Campo, B., André, S., Valmier, J., and Scamps, F. (2005). K^+ current regulates calcium-activated chloride current-induced after depolarization in axotomized sensory neurons. Eur. J. Neurosci. *22*, 1073–1080.

Huang, W.C., Xiao, S., Huang, F., Harfe, B.D., Jan, Y.N., and Jan, L.Y. (2012). Calcium-activated chloride channels (CaCCs) regulate action potential and synaptic response in hippocampal neurons. Neuron *74*, 179–192.

Jain, A., Huang, G.Z., and Woolley, C.S. (2019). Latent sex differences in molecular signaling that underlies excitatory synaptic potentiation in the hippocampus. J. Neurosci. *39*, 1552–1565.

Kanning, K.C., Kaplan, A., and Henderson, C.E. (2010). Motor neuron diversity in development and disease. Annu. Rev. Neurosci. *33*, 409–440.

Kaplan, A., Spiller, K.J., Towne, C., Kanning, K.C., Choe, G.T., Geber, A., Akay, T., Aebischer, P., and Henderson, C.E. (2014). Neuronal matrix metalloproteinase-9 is a determinant of selective neurodegeneration. Neuron *81*, 333–348.

Kunzelmann, K., Nilius, B., Owsianik, G., Schreiber, R., Ousingsawat, J., Sirianant, L., Wanitchakool, P., Bevers, E.M., and Heemskerk, J.W. (2014). Molecular functions of anoctamin 6 (TMEM16F): a chloride channel, cation channel, or phospholipid scramblase? Pflugers Arch. *466*, 407–414.

Leroy, F., Lamotte d'Incamps, B., Imhoff-Manuel, R.D., and Zytnicki, D. (2014). Early intrinsic hyperexcitability does not contribute to motoneuron degeneration in amyotrophic lateral sclerosis. eLife *3*, e04046.

Leroy, F., Lamotte d'Incamps, B., and Zytnicki, D. (2015). Potassium currents dynamically set the recruitment and firing properties of F-type motoneurons in neonatal mice. J. Neurophysiol. *114*, 1963–1973.

Liu, B., Linley, J.E., Du, X., Zhang, X., Ooi, L., Zhang, H., and Gamper, N. (2010). The acute nociceptive signals induced by bradykinin in rat sensory neurons are mediated by inhibition of M-type K^+ channels and activation of Ca^{2+}-activated Cl^- channels. J. Clin. Invest. *120*, 1240–1252.

Manuel, M., and Heckman, C.J. (2011). Adult mouse motor units develop almost all of their force in the subprimary range: a new all-or-none strategy for force recruitment? J. Neurosci. *31*, 15188–15194.

Martínez-Silva, M.L., Imhoff-Manuel, R.D., Sharma, A., Heckman, C.J., Shneider, N.A., Roselli, F., Zytnicki, D., and Manuel, M. (2018). Hypoexcitability precedes denervation in the large fast-contracting motor units in two unrelated mouse models of ALS. eLife *7*, e30955.

McCombe, P.A., and Henderson, R.D. (2010). Effects of gender in amyotrophic lateral sclerosis. Gend. Med. *7*, 557–570.

Miles, G.B., Hartley, R., Todd, A.J., and Brownstone, R.M. (2007). Spinal cholinergic interneurons regulate the excitability of motoneurons during locomotion. Proc. Natl. Acad. Sci. USA *104*, 2448–2453.

Müller, D., Cherukuri, P., Henningfeld, K., Poh, C.H., Wittler, L., Grote, P., Schlüter, O., Schmidt, J., Laborda, J., Bauer, S.R., et al. (2014). Dlk1 promotes a fast motor neuron biophysical signature required for peak force execution. Science *343*, 1264–1266.

Picollo, A., Malvezzi, M., and Accardi, A. (2015). TMEM16 proteins: unknown structure and confusing functions. J. Mol. Biol. *427*, 94–105.

Pun, S., Santos, A.F., Saxena, S., Xu, L., and Caroni, P. (2006). Selective vulnerability and pruning of phasic motoneuron axons in motoneuron disease alleviated by CNTF. Nat. Neurosci. *9*, 408–419.

Raoul, C., Estevez, A.G., Nishimune, H., Cleveland, D.W., deLapeyriere, O., Henderson, C.E., Haase, G., and Pettmann, B. (2002). Motoneuron death triggered by a specific pathway downstream of Fas. Potentiation by ALS-linked SOD1 mutations. Neuron *35*, 1067–1083.

Saxena, S., Cabuy, E., and Caroni, P. (2009). A role for motoneuron subtype-selective ER stress in disease manifestations of FALS mice. Nat. Neurosci. *12*, 627–636.

Saxena, S., Roselli, F., Singh, K., Leptien, K., Julien, J.P., Gros-Louis, F., and Caroni, P. (2013). Neuroprotection through excitability and mTOR required in ALS motoneurons to delay disease and extend survival. Neuron *80*, 80–96.

Schreiber, R., and Kunzelmann, K. (2016). Expression of anoctamins in retinal pigment epithelium (RPE). Pflugers Arch. *468*, 1921–1929.

Schroeder, B.C., Cheng, T., Jan, Y.N., and Jan, L.Y. (2008). Expression cloning of TMEM16A as a calcium-activated chloride channel subunit. Cell *134*, 1019–1029.

Van Den Bosch, L., Van Damme, P., Bogaert, E., and Robberecht, W. (2006). The role of excitotoxicity in the pathogenesis of amyotrophic lateral sclerosis. Biochim. Biophys. Acta *1762*, 1068–1082.

von Lewinski, F., and Keller, B.U. (2005). Ca^{2+}, mitochondria and selective motoneuron vulnerability: implications for ALS. Trends Neurosci. *28*, 494–500.

Woo, D.H., Han, K.S., Shim, J.W., Yoon, B.E., Kim, E., Bae, J.Y., Oh, S.J., Hwang, E.M., Marmorstein, A.D., Bae, Y.C., et al. (2012). TREK-1 and Best1 channels mediate fast and slow glutamate release in astrocytes upon GPCR activation. Cell *151*, 25–40.

Yang, Y.D., Cho, H., Koo, J.Y., Tak, M.H., Cho, Y., Shim, W.S., Park, S.P., Lee, J., Lee, B., Kim, B.M., et al. (2008). TMEM16A confers receptor-activated calcium-dependent chloride conductance. Nature *455*, 1210–1215.

Yang, H., Kim, A., David, T., Palmer, D., Jin, T., Tien, J., Huang, F., Cheng, T., Coughlin, S.R., Jan, Y.N., and Jan, L.Y. (2012). TMEM16F forms a Ca^{2+}-activated cation channel required for lipid scrambling in platelets during blood coagulation. Cell *151*, 111–122.

Zagoraiou, L., Akay, T., Martin, J.F., Brownstone, R.M., Jessell, T.M., and Miles, G.B. (2009). A cluster of cholinergic premotor interneurons modulates mouse locomotor activity. Neuron *64*, 645–662.

Zengel, J.E., Reid, S.A., Sypert, G.W., and Munson, J.B. (1985). Membrane electrical properties and prediction of motor-unit type of medial gastrocnemius motoneurons in the cat. J. Neurophysiol. *53*, 1323–1344.

Zhang, S.J., Zou, M., Lu, L., Lau, D., Ditzel, D.A., Delucinge-Vivier, C., Aso, Y., Descombes, P., and Bading, H. (2009). Nuclear calcium signaling controls expression of a large gene pool: identification of a gene program for acquired neuroprotection induced by synaptic activity. PLoS Genet. *5*, e1000604.

Zhang, Y., Zhang, Z., Xiao, S., Tien, J., Le, S., Le, T., Jan, L.Y., and Yang, H. (2017). Inferior olivary TMEM16B mediates cerebellar motor learning. Neuron *95*, 1103–1111.e4.

STAR★METHODS

KEY RESOURCES TABLE

REAGENT or RESOURCE	SOURCE	IDENTIFIER
Antibodies		
Rabbit polyclonal anti-ATF-3	Santa-Cruz Biotechnology	Cat#Sc-188; RRID: AB_2258513
Goat polyclonal anti-ChAT	Merck	Cat#AB144P; RRID: AB_2079751
Mouse monoclonal anti-ERRγ/NR3B3	R&D Systems	Cat#PP-H6812-00; RRID: AB_2100280
Rabbit polyclonal anti-MMP9	Abcam	Cat#ab38898; RRID: AB_776512
Mouse monoclonal anti-Na^+K^+-ATPase α1	Developmental Studies Hybridoma Bank	Cat#a6f; RRID: AB_528092
Mouse monoclonal anti-non-phosphorylated Neurofilament H (SMI-32)	Merck	Cat#NE1023; RRID: AB_2043449
Mouse monoclonal anti-Neurofilament M	Developmental Studies Hybridoma Bank	Cat#2H3; RRID: AB_2314897
Mouse monoclonal anti-p75 (clone MLR2)	Merck	Cat#MAB5592; RRID: AB_570558
Mouse monoclonal anti-Synaptic vesicle glycoprotein 2A	Developmental Studies Hybridoma Bank	Cat#SV2; RRID: AB_2315387
Mouse monoclonal anti-Synaptobrevin2/VAMP2 (clone 69.1)	Synaptic Systems	Cat#104211 ; RRID: AB_887808
Mouse monoclonal anti-Synaptophysin	Merck	Cat#MAB5258: RRID: AB_11214259
Rabbit polyclonal anti-TMEM16F	Yang et al., 2012	N/A
Rabbit polyclonal anti-TMEM16F	Aviva systems biology	Cat#ARP44759-P050 ; RRID: AB_10882053
Rabbit polyclonal anti-TMEM16F (C-terminal)	Schreiber and Kunzelmann, 2016	N/A
Goat polyclonal anti-VAChT	Merck	Cat#ABN100; RRID: AB_2630394
Guinea pig polyclonal anti-VGluT1	Merck	Cat#AB5905; RRID: AB_2301751
Guinea pig polyclonal anti-VGluT2	Synaptic Systems	Cat#135404; RRID: AB_887884
Chemicals, Peptides, and Recombinant Proteins		
Human BDNF	ImmunoTools	Cat#11343373
Rat GDNF	Sigma-Aldrich	Cat#G1401
Rat CNTF	R&D systems	Cat# 557-NT-050/CF
Hydroxystilbamidine, methanesulfonate	ThermoFisher Scientific	Cat#H22845
Niflumic acid	Sigma-Aldrich	Cat#N0630
Oxotremorine M	Sigma-Aldrich	Cat#O100
Alpha-bungarotoxin, Alexa Fluor 555 conjugate	ThermoFisher Scientific	Cat#B35451
Critical Commercial Assays		
RNeasy Mini Kit	QIAGEN	Cat#74104
RNAprotect Tissue Reagent	QIAGEN	Cat#76104
QuantiTect Reverse Transcription kit	QIAGEN	Cat#205311
NucleoSpin extract II kit	Macherey-Nagel	Cat#740955
BigDye Terminator v1.1 Cycle Sequencing kit	ThermoFisher Scientific	Cat#4337452
Agencourt CleanSEQ kit	Beckman Coulter	Cat#A29151
Experimental Models: Cell Lines		
Human HEK293T	ATCC	CRL11268
Experimental Models: Organisms/Strains		
Mouse: B6.Cg-Tg(SOD1*G93A)1Gur/J	The Jackson Laboratory	Stock No. 004435
Mouse: B6.Cg-Tg(Hlxb9-GFP)1Tmj/J	The Jackson Laboratory	Stock No. 005029
Mouse: C57BL/6-Tmem16−/−	Yang et al., 2012	N/A

(*Continued on next page*)

Continued

REAGENT or RESOURCE	SOURCE	IDENTIFIER
Oligonucleotides		
Primer Tmem16a Forward: TTCGTCAATCACACGCTCTC	This paper	N/A
Primer Tmem16a Reverse: GGGGTTCCCGGTAATCTTTA	This paper	N/A
Primer Tmem16b Forward: CGCATGCACTTTCACGACAA	This paper	N/A
Primer Tmem16b Reverse: ATCCAGTGGCCCAAGTTCAA	This paper	N/A
Primer Tmem16c Forward: TTGGGAAGATTCGTAGGCCA	This paper	N/A
Primer Tmem16c Reverse: TGTGTCGTGACCACCAGTTT	This paper	N/A
Primer Tmem16d Forward: ATCCATCAACGGCGAAGTGT	This paper	N/A
Primer Tmem16d Reverse: TTATTGACCGTCTGCCTGGT	This paper	N/A
Primer Tmem16e Forward: TTGCAAGAACTGGGCTCGAT	This paper	N/A
Primer Tmem16e Reverse: GAGCCGCAAACAACAGCATT	This paper	N/A
Primer Tmem16f Forward: TCTGGTGCTGGAAAACTTTGA	This paper	N/A
Primer Tmem16f Reverse: TCGGGCTTCCCGTTAAATTC	This paper	N/A
Primer Tmem16 g Forward: TCCTCAATTTCACGCTGGCA	This paper	N/A
Primer Tmem16 g Reverse: AGAACACGGCCAATGGAGAA	This paper	N/A
Primer Tmem16h Forward: CACAAGGCATGGATGAAGACA	This paper	N/A
Primer Tmem16h Reverse: GTATGTGGCGGTGACAAAGAA	This paper	N/A
Primer Tmem16j Forward: TGCCATCTTCATGGCACTGT	This paper	N/A
Primer Tmem16j Reverse: TGACGGTGGTCTTTCAGCTT	This paper	N/A
Primer Tmem16k Forward: TCCTGAATTGCTTCGCCTC	This paper	N/A
Primer Tmem16k Reverse: AATGCCTGAACCTTCCGCTT	This paper	N/A
Primer Polr2J Forward: ACCACACTCTGGGGAACATC	Bowerman et al., 2017	N/A
Primer Polr2J Reverse: CTCGCTGATGAGGTCTGTGA	Bowerman et al., 2017	N/A
Primer Gapdh Forward: GGGTTCCTATAAATACGGACTGC	This paper	N/A
Primer Gapdh Reverse: TACGGCCAAATCCGTTCACA	This paper	N/A
Primer Tmem16f exon 1 Forward: TGACTAGGAAGGTCCTGCTGA	This paper	N/A
Primer Tmem16f exon 6 Reverse: TCATTCATCCGGCTCTTCTC	This paper	N/A
Primer Tmem16f exon 2 Forward: ACTCCAGGAGGCCTTTTCTG	This paper	N/A
Primer Tmem16f exon 19 Forward: ACCCATACATTGGGCTTGGT	This paper	N/A
Primer Tmem16f exon 20 Reverse: CGGCAATCACGTGCCAATAG	This paper	N/A
siRNA targeting sequence: Tmem16a #1: CGGUCCAACAUCCGGGUUA	Horizon Discovery	SMARTpool
siRNA targeting sequence: Tmem16a #2: CCAGAAACAAAGAGACCGA	Horizon Discovery	SMARTpool
siRNA targeting sequence: Tmem16a #3: UAUAAAGAUUACCGGGAAC	Horizon Discovery	SMARTpool
siRNA targeting sequence: Tmem16a #4: GCAGAAUGGUACCUAGGAA	Horizon Discovery	SMARTpool
siRNA targeting sequence: Tmem16b #1: GUUCAAAGAUUAUCGAGAA	Horizon Discovery	SMARTpool
siRNA targeting sequence: Tmem16b #2: CCGCAUUGUACACGAGAUU	Horizon Discovery	SMARTpool
siRNA targeting sequence: Tmem16b #3: CCAAGAAAAUGUACGAGAU	Horizon Discovery	SMARTpool

(*Continued on next page*)

Continued

REAGENT or RESOURCE	SOURCE	IDENTIFIER
siRNA targeting sequence: Tmem16b #4: ACGCAUGAGUACACCAUAU	Horizon Discovery	SMARTpool
siRNA targeting sequence: Tmem16c #1: GAUAACAACUGAAGCGUCA	Horizon Discovery	SMARTpool
siRNA targeting sequence: Tmem16c #2: CAAGUGGAAUUUCGUCAAA	Horizon Discovery	SMARTpool
siRNA targeting sequence: Tmem16c #3: GAUUAGUCACAAUGAACGA	Horizon Discovery	SMARTpool
siRNA targeting sequence: Tmem16c #4: CAAAAGUGGGUAUCCGUAA	Horizon Discovery	SMARTpool
siRNA targeting sequence: Tmem16d #1: CCUAUGGACUCUUCGAUGA	Horizon Discovery	SMARTpool
siRNA targeting sequence: Tmem16d #2: GAUCUAAGGGACCGGAUGA	Horizon Discovery	SMARTpool
siRNA targeting sequence: Tmem16d #3: CGAGCAAGCAUGCACGUUA	Horizon Discovery	SMARTpool
siRNA targeting sequence: Tmem16d #4: GAACUUGGCUACCCGUUAA	Horizon Discovery	SMARTpool
siRNA targeting sequence: Tmem16f #1: ACAUCAAACUCCCGCUAAA	Horizon Discovery	SMARTpool
siRNA targeting sequence: Tmem16f #2: AGAAAUACCUCACGCAGAA	Horizon Discovery	SMARTpool
siRNA targeting sequence: Tmem16f #3: GAAUCUAAUUGGACGAUAU	Horizon Discovery	SMARTpool
siRNA targeting sequence: Tmem16f #4: GGGCAAAUACAGAAGCGAA	Horizon Discovery	SMARTpool
siRNA targeting sequence: Tmem16h #1: CCAUCGUGGUAAACUGCUA	Horizon Discovery	SMARTpool
siRNA targeting sequence: Tmem16h #2: ACGAGGAAUACGAGGGCGA	Horizon Discovery	SMARTpool
siRNA targeting sequence: Tmem16h #3: GUGGCAAGGAGGAGGACGA	Horizon Discovery	SMARTpool
siRNA targeting sequence: Tmem16h #4: GAGCUGGGCUUGCGAACCA	Horizon Discovery	SMARTpool
siRNA targeting sequence: Tmem16k #1: CAUUAAAGUCUGAGGUCGA	Horizon Discovery	SMARTpool
siRNA targeting sequence: Tmem16k #2: GUGCGAGGGUAAAGCGGAA	Horizon Discovery	SMARTpool
siRNA targeting sequence: Tmem16k #3: GGGCAGAAGCAGUCGGUCU	Horizon Discovery	SMARTpool
siRNA targeting sequence: Tmem16k #4: CUUACUGGCUGCAGCGGAA	Horizon Discovery	SMARTpool
siRNA control: UGGUUUACAUGUCGACUAA	Horizon Discovery	SMARTpool
mAno6-Forward: TGTAAAACGACGGCCAGTA GCGCCTGCTGAAGCAGA	This paper	N/A
mAno6-Reverse: GGATAACAATTTCACACAGGG CGCGTGCACTTTTACGA	This paper	N/A
Sequencing primer M13 Forward: TGTAAAACGACGGCCAGT	This paper	N/A
Sequencing primer M13 Reverse: GGATAACAATTTCACACAGG	This paper	N/A

(*Continued on next page*)

Continued

REAGENT or RESOURCE	SOURCE	IDENTIFIER
Recombinant DNA		
pCMV-Tmem16F (variant 1)-IRES2-mCherry	GeneCopoeia	EX-Mm33601-Lv214
pCMV-Tmem16f (variant 2)-IRES2-mCherry	GeneCopoeia	EX-Mm12997-Lv214
pCMV-IRES2-mCherry	GeneCopoeia	EX-NEG-Lv214
Software and Algorithms		
pClamp10	Molecular Device	https://www.moleculardevices.com
ImageJ	National Institutes of Health, USA	https://imagej.nih.gov/ij/
Primer-BLAST	National Center for Biotechnology Information	https://www.ncbi.nlm.nih.gov/tools/primer-blast/
ACTITRACK	BioSeb	https://www.bioseb.com/bioseb/anglais/default/index.php
CatWalk 7.1	Noldus	https://www.noldus.com/
SEDACOM	Panlab Harvard Apparatus	https://www.panlab.com/en/
Prism	GraphPad	https://www.graphpad.com
Zen	Zeiss	https://www.zeiss.com/corporate/int/home.html
Imaris	Oxford Instruments	https://imaris.oxinst.com

LEAD CONTACT AND MATERIALS AVAILABILITY

Further information and requests for resources and reagents should be directed to and will be fulfilled by the Lead Contact, Frédérique Scamps (frederique.scamps@inserm.fr). This study did not generate new unique reagents.

EXPERIMENTAL MODEL AND SUBJECT DETAILS

Animals

All animal experiments were approved by the national ethics committee on animal experimentation, and were done in compliance with the European community and national directives for the care and use of laboratory animals. B6.Cg-Tg(SOD1*G93A)1Gur/J (*SOD1*^{G93A}) were purchased from the Jackson Laboratory. *Hb9::GFP* mice were obtained from T.M. Jessell's laboratory (Columbia University, NY, USA) and are available at the Jackson Laboratory (B6.Cg-Tg(Hlxb9-GFP)1Tmj/J). *Tmem16f*$^{-/-}$ mice were obtained from Dr. Lily Y Jan (UCLA University). Mice were maintained on a C57BL/6J background under specific-pathogen-free conditions and housed in cages with a 12 h light/12 h dark cycle, with food and water supplied *ad libitum*. For all experiments, the age of mice is indicated in the main text, figure legends or figures. Unless otherwise indicated, mixed-sex cohorts of mice per experimental group were used.

Cell Line

The human embryonic kidney 293T (HEK293T) cell line was used in this study.

METHOD DETAILS

Motoneuron culture

Motoneurons were isolated from the ventral spinal cord of E12.5 mice embryos as described previously (Raoul et al., 2002). Briefly, cells were dissociated mechanically after trypsin treatment of the spinal cords. The largest cells were isolated using iodixanol density gradient centrifugation. To purify motoneurons, we added an immuno-purification step using magnetic cell isolation technology (Arce et al., 1999). Briefly, cells were collected at the iodixanol interface and centrifuged through a BSA cushion. Isolated neurons were then incubated at +4°C in 80 μl of L-15 medium containing 0.5% BSA and 2 μl of anti-mouse p75 monoclonal antibody (Clone MLR2, Millipore) for 20 min, followed, after centrifugation through a BSA cushion, by a 15 min incubation in 80 μl of L-15 medium containing 0.5% BSA and 10 μl of microbead-conjugated goat anti-mouse IgG (Miltenyi Biotec). Cells were centrifuged, collected in L-15 containing 0.5% BSA and applied onto a column for magnetic cell separation (Miltenyi Biotec). After wash-out of the negative fraction with L15/BSA, cells were collected and centrifuged through BSA cushion. Motoneurons were plated onto poly-ornithine laminin-coated 4-well plates at the density of 2,500 per well in the presence of a cocktail of neurotrophic factors including glial-derived neurotrophic factor (GDNF, 0.1 ng/ml), brain-derived neurotrophic factor (BDNF, 1 ng/ml) and ciliary neurotrophic factor (CNTF, 10 ng/ml) in

supplemented Neurobasal medium (2% (vol/vol) horse serum, 2% (vol/vol) B27 supplement (ThermoFisher Scientific), 50 μM L-glutamine, 25 μM L-glutamate, 25 μM 2β-mercaptoethanol and 0.5% penicillin/streptomycin). Using *Hb9::*GFP embryos to trace motoneurons, we found that this protocol yielded approximately 90% of GFP-positive neurons.

Spinal cord slice preparation

Spinal cord slices were prepared from post-natal day 7 (P7)-P11 mice. One day before experiments, mice received intraperitoneal injections of hydroxystilbamidine, methanesulfonate (Fluoro-gold; 0.04 mg/g weight; ThermoFisher Scientific) to retrogradely label motoneurons (Miles et al., 2007). The spinal cord was dissected in ice cold dissection solution containing (in mM): 190 sucrose, 20 dextrose, 25 $NaHCO_3$, 1.25 KH_2PO_4, 0.75 K-gluconate, 1 $CaCl_2$, 4 $MgSO_4$, 3 myo-inositol, 5 Na-pyruvate and 1 L-ascorbic acid, continuously bubbled with 95% O2 and 5% CO_2 to a final pH of 7.4 (osmolarity, 297-307 mOsm). After cutting caudal and cervical part, the spinal cord was embedded in a 3% (wt/vol) low melt agarose solution. The agarose block was placed at 4°C and then glued upright to the vibratome stage and 280 μm transverse slices of lumbar cord were cut (Leica VT1200S) in ice cold dissection solution. Slices were kept at 32°C in spinal cord recording solution complemented with (mM) 3 myo-inositol, 5 Na-pyruvate, and 1 L-ascorbic acid.

Electrophysiological recordings

CaCC in motoneurons were recorded between 7 and 10 days *in vitro* (DIV). siRNA transfected neurons were recorded 48 h after electroporation. Whole cell patch-clamp recordings were done at room temperature under conditions optimized for the isolation of Ca^{2+} and Cl^- currents separately from other voltage-activated currents. The bathing solution contains (in mM): 145 N-Methyl-D-Glucamine, 2 $CaCl_2$, 1.5 $MgCl_2$, 10 HEPES and 10 glucose, and the pH was adjusted to 7.4 with HCl. Osmolarity was 300 ± 5 mOsm. Recording pipettes were filled with the following solution (in mM): 145 CsCl (high $[Cl^-]_i$) or 10 mM CsCl-145 Cs-methane sulfonate (low $[Cl^-]_i$), 10 HEPES, 2 Mg-ATP, 0.5 Na_2-GTP, and pH 7.35 adjusted with CsOH. Osmolarity was 295-300 mOsm. All recordings were made at room temperature using an Axopatch 200B amplifier and a Digidata 1322A A/D board (Molecular Devices) and acquired at 5 kHz.

For electrical activity measurements, spinal cord slices were perfused at 1.5 ml/min heated at 32°C with the following recording solution (in mM): 115 NaCl, 2.5 KCl, 25 $NaHCO_3$, 1.25 NaH_2PO_4, 1.5 $MgCl_2$, 2.5 $CaCl_2$, 10 glucose (95% O_2-5% CO_2 final pH 7.4; 300 mOsm). Whole-cell configuration was used for motoneuron recordings with 3-6 MΩ patch pipettes containing (in mM) 10 KCl, 135 K-methane-sulfonate, 1.5 Mg-ATP, 0.5 Na-GTP, 0.1 EGTA and 10 HEPES, adjusted to pH 7.35. According to gramicidin-based measurements performed in motoneurons from neonatal mouse spinal cord slices, $[Cl^-]_i$ was set at 10 mM (Delpy et al., 2008). Recordings were performed with a Multiclamp 700B amplifier, acquired at 10 kHz by using a Digidata 1550A A/D board and pClamp10 software (Molecular Devices). Following whole-cell configuration, input resistance, Rin and cell capacity, Cm, of Fluoro-gold positive motoneurons were automatically calculated under voltage-clamp using 100 ms, 10 mV depolarization steps from - 70 mV holding potential. Niflumic acid (NFA), oxotremorine were purchased from Sigma-Aldrich.

RNA extraction and RT-qPCR

For primary cultures, total mRNA was extracted from roughly 30,000 immunopurified embryonic motoneurons at 7 DIV with the RNeasy Mini Kit (QIAGEN). For P30 lumbar spinal cords, the tissues were harvested in RNAprotect Tissue Reagent (QIAGEN). Lysis buffer was used for pestle tissue crushing and homogenization by passing the lysate through needles. Lysates were then mixed with an equal volume of 70% ethanol, and total mRNA was separated from other cellular components on RNeasy minispin columns. The eluted mRNA was quantified by spectrophotometry (Nanodrop 2000, ThermoFisher Scientific). Following genomic DNA wipe out, reverse transcription was performed with 100 ng to 1 μg of mRNA with the Quantitect RT kit (QIAGEN). The collected cDNA was diluted to 50 ng (culture) or 100 ng (tissue) in H_20 and stored at −20°C until use. Primers were designed with Primer-BLAST software. Quantitative PCR was performed on 5 or 10 ng cDNA with SYBR Green (QIAGEN) for detection and the LightCycler system (Roche Diagnostics). After initial activation for 15 min at 95°C, 45 cycles of 94°C for 15 s, 60°C for 20 s and 72°C for 35 s were carried out. After PCR amplification, a melting curve analysis was carried out to check PCR specificity. *Polr2J* and *Gapdh* levels were used to normalize the amounts of cDNA. ΔC_t was calculated as the differences between the Ct values, determined with the Equation 2–ΔCt. Primer sequences are given in the Key Resources Table.

RNA interference Experiments

Pooled specific siRNA against mouse *Tmem16* or non-targeting control siRNA were the ON-TARGETplus SMARTpools from Dharmacon Horizon Discovery (siRNA sequences are given in the Key Resources Table). *Hb9*::*GFP* motoneurons at 6-7 DIV were individually electroporated as we previously described (Boudes et al., 2008). Electrode tips were filled with 8 μl 145 mM KCl, 10 mM HEPES containing dextran-rhodamine (3 mM)/siRNA (1 μM) and 10 V, 1 ms negative current pulses were delivered at 100 Hz for 1 s (Axoporator 800A, Molecular Devices).

Sequencing

The primers used for PCR were: mAno6-Forward: TGTAAAACGACGGCCAGTAGCGCCTGCTGAAGCAGA (in exon 1) and mAno6-Reverse: GGATAACAATTTCACACAGGGCGCGTGCACTTTTACGA (in exon 6). The PCR products were extracted from bands on

agarose gels (NucleoSpin extractII kit, Macherey-Nagel) and were sequenced with the following primers: M13-Forward: TGTAAAAC-GACGGCCAGT and M13-Reverse: GGATAACAATTTCACACAGG. Sequencing reactions were carried out with the BigDye® Terminator v1.1 Cycle Sequencing Kit (Applied Biosystems, ThermoFisher Scientifc) and products were purified with the CleanSEQ kit (Beckman Coulter Genomics), according to the manufacturer's instructions. The purified products were finally resolved on a 3130xl Genetic Analyzer (Applied Biosystems).

TMEM16F expression vector and transfection

Expression vector containing the coding sequence for mouse *Tmem16f* variant 1 (GenBank accession number NM_001253813) and variant 2 (GenBank accession number NM_175344) was obtained from GeneCopoeia (Rockville, MD, USA). Plasmids incorporate cytomegalovirus promoter and an internal ribosome entry site (IRES2) sequence coupling mCherry expression to TMEM16F. Human embryonic kidney 293T (HEK293T) were maintained in DMEM containing 10% fetal calf serum, 100 U/ml penicillin and 100 μg/ml streptomycin. Plasmids were transfected using Lipofectamine 2000 reagent according to manufacturer's instructions (ThermoFisher Scientific).

Immunohistochemistry

For spinal cord, mice were anaesthetized and transcardially perfused with 4% paraformaldehyde in phosphate-buffered saline (PBS). Lumbar spinal cord was removed and post-fixed in 4% paraformaldehyde, dehydrated in 30% sucrose solution, flash-frozen and cut at a 18 μm thickness. For TMEM16F immunohistochemistry experiments, a citrate buffer antigen retrieval step was performed. The sections were then rinsed 5 min with PBS and incubated for 2 h at room temperature in blocking solution (Tris-buffered saline, 0.9% L-Lysine, 20% donkey serum, 0.3% Triton X-100). This was followed by an overnight incubation at +4°C with primary antibodies (see Key Resources Table). Subsequently, sections were incubated 1 h with appropriate Alexa Fluor secondary antibodies (ThermoFisher Scientifc). All washes were done with PBS. Slides were mounted in Mowiol.

For neuromuscular junctions, *tibialis anterior* muscle was dissected and fixed in 4% paraformaldehyde for 15 min. Muscle was placed in 30% sucrose solution, flash-frozen and cut at a 30 μm thickness. The sections were then rinsed 5 min in PBS and incubated for 2 h at room temperature in blocking solution (Tris-buffered saline, 2% bovine serum albumin, 0.5% Triton X-100). This was followed by an overnight incubation at +4°C with the primary antibodies. Subsequently, sections were rinsed in PBS, 2% bovine serum albumin and incubated 1 h with the secondary antibodies and αBTX-Alexa Fluor 555 conjugate (ThermoFisher Scientific). Sections were washed in PBS and slides were mounted in Mowiol. Image acquisition were done using Zeiss confocal microscope with Zen software (Zeiss). ImageJ (National Institutes of Health, USA) was used for synaptic quantifications. Image reconstruction from confocal z stack fluorescence images of spinal cord was done using Imaris software (Oxford Instruments).

Functional tests

Locomotor activity-open field. Mice were placed in a wall-enclosed arena and the spontaneous locomotion was acquired for 10 min using an infrared actimeter (Bioseb) and analyzed with the ACTITRACK tracking software (Bioseb).

Walking track analysis

To assess gait analysis, we used the CatWalk (Noldus Information Technology). Briefly, animals crossing the walkway with a glass floor were videotaped using a computer-assisted setup and digitized data of paw-floor contact area are used for offline analysis. A normal run was defined as: the mouse crossing the walkway without any interruptions or hitches, the presence of footfall patterns for all four pads, and a running time of around one second to cover 45 cm. Three consecutive runs were recorded. Static parameters (intensity of the paw prints, print width and print length) and dynamic parameters (stance phase, swing phase, swing speed and duty cycle) were measured using CatWalk software 7.1.

Treadmill

Mice were exercised using LE8710MTS treadmill (Bioseb). For two days, animals were habituated to the treadmill by placing them on an unmoving 0° inclined treadmill for 10 min, then at 5 cm/s for 10 min, and at 10 cm/s for 10 min with electrical stimulus to motivate them. On the exercise testing day, animals ran on the treadmill with a 10° inclination. After a low-speed warm-up (15 cm/s for 5 min), mice were subjected to an incrementally increasing running speed. Every 20 s, the speed was increased by 5 cm/s until the mice was exhausted. The criterion of exhaustion was defined as the inability of the animal to run on the treadmill despite a 10 s electrical stimulus. The fastest speed that a mouse could run was recorded as its maximal running speed. The day after, both WT and *Tmem16f*$^{-/-}$ mice ran at 60% of the average maximal speed of WT mice for 20 min or until mice were exhausted. Run data were collected with SEDACOM software.

Grid test

For muscle strength analysis, we measured the time mice held a grid before dropping it, with a plateau of 30 s, starting with a 40 g metal grid (followed by 30, 20 and 10 g grids). The experiment was repeated three times with each grid. Muscle strength (arbitrary units) was quantified with the following formula: (40 g x best time) + (30 g x best time) + (20 g x best time) + (10 g x best time). Mice were evaluated weekly starting at 56 days.

Weight curves

Mice were weighed weekly starting at 28 days of age and thrice weekly starting at 56 days of age.

Life expectancy

mortality was defined as the point in time when the mice are unable to right themselves within 15 s after being placed upon their back.

QUANTIFICATION AND STATISTICAL ANALYSIS

All histograms show mean values ± standard error of the mean (SEM). All experiments were done at least three times independently. Statistical significance was determined when appropriate by paired or unpaired two-tailed t test, Mann-Whitney test, one-way analysis of variance (ANOVA) followed by Dunnett's or Tukey-Kramer's post hoc test and two-way repeated-measure ANOVA followed by a Newman-Keuls's post hoc test. For the Kaplan-Meier survival analysis, the Log-rank test was used. Statistical parameters (including the number of recorded cells, mice, sections, independent experiments…) were reported in the figure legend. Statistical analyses were done with Prism software version 7 (GraphPad Software). Significance was accepted at the level of $p < 0.05$.

DATA AND CODE AVAILABILITY

This study did not generate any unique datasets or code.